

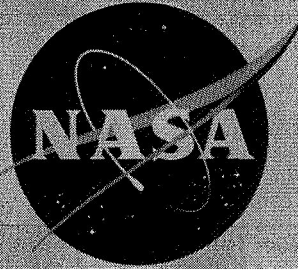
62 10030

Copy

573

NASA TM X-689

NASA TM X-689

CLASSIFICATION CHANGED  
UNCLASSIFIEDTO  
By Authority of NASA 10/30/70

## TECHNICAL MEMORANDUM

X-689

TRANSONIC STABILITY OF A PRELIMINARY  
VERTICAL-TAKE-OFF LAUNCH CONFIGURATION WITH A  
HORIZONTAL-LANDING RECOVERABLE BOOSTER

By P. Kenneth Pierpont

Langley Research Center  
Langley Station, Hampton, Va.Declassified by authority of NASA  
Classification Change Notices No. 211  
Dated \*\* 10/30/70

FACILITY FORM 602

N71-70287	
(ACCESSION NUMBER)	(THRU)
43	None
(PAGES)	(CODE)
(NASA CR OR TMX OR AD NUMBER)	(CATEGORY)

NATIONAL AERONAUTICS AND SPACE ADMINISTRATION  
WASHINGTON  
May 1962

CONFIDENTIAL

## NATIONAL AERONAUTICS AND SPACE ADMINISTRATION

TECHNICAL MEMORANDUM X-689

TRANSONIC STABILITY OF A PRELIMINARY  
VERTICAL-TAKE-OFF LAUNCH CONFIGURATION WITH A  
HORIZONTAL-LANDING RECOVERABLE BOOSTER\*

By P. Kenneth Pierpont

## SUMMARY

An investigation has been made of a model of a preliminary three-stage launch configuration with a horizontal-landing recoverable booster in the Langley 8-foot transonic pressure tunnel. The stability of both the launch vehicle, with either a ballistic spacecraft or a winged spacecraft, and the recoverable booster alone was determined over a Mach number range from 0.6 to 1.2 and at angles of attack up to  $14^\circ$ . Test Reynolds numbers varied from about  $3.2 \times 10^6$  to  $4.2 \times 10^6$  per foot.

The winged spacecraft caused significant destabilizing increments which may require the use of both aerodynamic controls and engine gimbaling if the same launch vehicle is to be used for both ballistic and winged spacecraft. The recoverable booster alone was stable longitudinally and directionally but the drag of the large base area caused appreciable reductions in the maximum lift-drag ratio, and thus in the power-off glide range. This problem might be alleviated if boattailing or venting of the base could be achieved.

## INTRODUCTION

Compliance with demands for placing both increased payloads in orbit and increased launch frequency for such payloads will place a severe drain on the economy and the productive capacity of this country. One possible method for improving the cost per pound in orbit as well as increasing the launch-frequency potential lies in the utilization of a recoverable booster system. The use of a fixed-wing vertical-take-off-and-horizontal-landing recoverable booster would minimize recovery damage, would allow return and recovery at the launch site, or alternatively down range, and might allow ferrying of the booster from the manufacturer to the launch site by either powered

or towed means. In addition, improved reliability might result from complete postflight inspection of the recoverable stage. Therefore, an investigation has been initiated to study some of the aerodynamic problems associated with the application of vertical-take-off-and-horizontal-landing (VTOHL) recoverable boosters.

An existing research model was modified to simulate a two-stage launch vehicle with different upper-stage configurations. A tandem stage arrangement was selected for these tests. Two types of upper stages were investigated, a simple ballistic nose cone and a winged rocket stage, to simulate two possible extremes of upper stages. The overall investigation is intended to provide aerodynamic data for the complete vehicle as well as the recoverable booster itself throughout the transonic and hypersonic speed ranges. Only the results of the transonic tests are presented herein.

L  
1  
9  
3  
4

The tests were made in the Langley 8-foot transonic pressure tunnel over a Mach number range from 0.6 to 1.2 and at angles of attack from about  $-2^{\circ}$  to  $14^{\circ}$ . A nominal amount of data has been included at  $5^{\circ}$  sideslip. Test Reynolds numbers ranged from about  $3.2 \times 10^6$  to  $4.2 \times 10^6$  per foot.

#### SYMBOLS

$C_N$  normal-force coefficient,  $\frac{\text{Normal force}}{qS}$

$C_A$  axial-force coefficient,  $\frac{\text{Axial force}}{qS}$

$C_L$  lift coefficient,  $\frac{\text{Lift}}{qS}$

$C_D$  drag coefficient,  $\frac{\text{Drag}}{qS}$

$C_m$  pitching-moment coefficient referred to  $0.25\bar{c}$ ,  $\frac{\text{Pitching moment}}{qS\bar{c}}$

$C_l$  rolling-moment coefficient,  $\frac{\text{Rolling moment}}{qSb}$

$C_n$	yawing-moment coefficient referred to $0.25\bar{c}$ , $\frac{\text{Yawing moment}}{qSb}$
$C_Y$	side-force coefficient, $\frac{\text{Side force}}{qS}$
$C_{L\alpha}$	lift-curve slope, $\frac{\partial C_L}{\partial \alpha}$ , per deg
$C_{mC_L}$	longitudinal-stability parameter (stability axes), $\frac{\partial C_m}{\partial C_L}$
$C_{mC_N}$	longitudinal-stability parameter (body axes), $\frac{\partial C_m}{\partial C_N}$
$C_{l\beta}$	effective-dihedral parameter, $\frac{\Delta C_l}{\Delta \beta}$ , per deg
$C_{n\beta}$	directional-stability parameter, $\frac{\Delta C_n}{\Delta \beta}$ , per deg
$C_{Y\beta}$	side-force parameter, $\frac{\Delta C_Y}{\Delta \beta}$ , per deg
$L/D$	lift-drag ratio, $\frac{C_L}{C_D}$
$b$	wing span, in.
$c$	chord, in.
$\bar{c}$	mean aerodynamic chord of recoverable booster, in.
$M$	free-stream Mach number
$q$	free-stream dynamic pressure, lb/sq ft
$R$	Reynolds number per foot

4

S wing area, sq ft

$\frac{x_{ac}}{c}$  aerodynamic-center location

$\frac{x_{cp}}{c}$  center-of-pressure location

$\alpha$  angle of attack, deg

$\beta$  angle of sideslip, deg

Subscripts:

b condition at model base

o condition at zero angle of attack or zero lift

max maximum

## MODEL DESCRIPTION

The model consisted of a first-stage winged recoverable booster, a second-stage expendable booster, and a spacecraft; all three stages were arranged in tandem. The general arrangement of the launch configuration with the winged spacecraft is shown in figure 1(a) and the first-stage recoverable booster alone is shown in figure 1(b). The wing of the first-stage booster, shown in figure 1(c), was a simple wedge-slab of 2-percent thickness rearward of the 40-percent-chord station and had a delta planform with 70° of leading-edge sweep. The wing was designed to provide an estimated wing loading of 40 pounds per square foot at landing conditions. The resulting wing span was about 5.5 body diameters, and the mean aerodynamic chord based on the total wing area was 12.69 inches. The vertical tail was a half-delta planform having 70° of leading-edge sweep and its area was 12.5 percent of the wing area. The first-stage booster had a length-diameter ratio of approximately 6, excluding the interstage fairing which was about 1.5 diameters long. The ratio of second-stage diameter to first-stage diameter was 0.95, and the length-diameter ratio of the second stage was 5.5, excluding the interstage fairing. The moment reference was chosen to be the 0.25c station of the recoverable first stage, since the first stage must function as an airplane during its return flight.

The two spacecraft configurations tested were a ballistic nose (consisting of a  $40^\circ$  blunted cone) and a winged spacecraft (consisting of a simple  $70^\circ$  slab delta wing with semicircular leading edges which was mounted on a cylindrical body). Details of the recoverable-booster wing and vertical fin and of the two spacecraft are shown in figure 1(c).

Photographs of the model configurations are shown in figure 2. The model dimensions are given in table I.

### APPARATUS AND TESTS

The tests were made in the Langley 8-foot transonic pressure tunnel over a range of Mach numbers from 0.6 to 1.2, and at angles of attack from about  $-2^\circ$  to  $14^\circ$ . Some data were obtained over the angle-of-attack range at a sideslip angle of  $5^\circ$ . The test Reynolds number per foot ranged from about  $3.2 \times 10^6$  to  $4.2 \times 10^6$ . (See fig. 3.)

Six-component force and moment data were obtained by means of an internally mounted strain-gage balance. Angles of attack and sideslip were corrected for balance and sting deflections under load. The axial force was corrected to correspond to a base pressure equal to the free-stream static pressure except where specifically noted.

The accuracy of the data has been estimated on the basis of repeatability of data and balance accuracy to be approximately as follows:

M . . . . .	$\pm 0.005$
$\alpha$ , deg . . . . .	$\pm 0.1$
$C_N$ . . . . .	$\pm 0.01$
$C_A$ . . . . .	$\pm 0.001$
$C_m$ . . . . .	$\pm 0.002$
$C_l$ . . . . .	$\pm 0.001$
$C_n$ . . . . .	$\pm 0.001$
$C_y$ . . . . .	$\pm 0.002$

### PRESENTATION OF RESULTS

The results of this investigation have been reduced to coefficient and parameter form. The characteristics of the complete launch configurations are considered first, and then the characteristics of the first-stage recoverable booster alone.

The launch configuration comprised the first-stage recoverable booster, the second-stage expendable booster, and the final spacecraft stage. The aerodynamic characteristics for the launch configuration are referred to the body axes with the quarter chord of the mean aerodynamic chord of the first-stage wing as the moment reference. The moment reference is 9.52 inches forward of the model base (table I). Figures pertaining to this part of the investigation are as follows:

	Figure	
Longitudinal aerodynamic characteristics of the launch vehicle with a ballistic and a winged spacecraft. $\beta = 0^\circ$ . . . . .	4	L 1 9 3 4
Aerodynamic characteristics of the launch vehicle with winged spacecraft. $\beta = 0^\circ$ and $5^\circ$ . . . . .	5	
Variation of the axial-force coefficient and longitudinal stability parameter for the launch vehicle with ballistic and winged spacecraft. $\alpha = 0^\circ$ . . . . .	6	
Variation of the center-of-pressure location with angle of attack for the launch vehicle with ballistic and winged spacecraft . . . . .	7	
Effect of angle of attack on the variation of the lateral-directional stability parameters with Mach number for the launch vehicle with winged spacecraft . . . . .	8	

The second part of the presentation consists of the aerodynamic characteristics for the first-stage recoverable booster alone. The longitudinal data are referred to the stability axes, since this configuration represents an airplane, whereas the lateral-directional data are referred to the body axes. The moment reference is the quarter chord of the mean aerodynamic chord of the total wing area. Figures pertaining to this part of the investigation are as follows:

	Figure
Aerodynamic characteristics of the recoverable booster alone at $\beta = 0^\circ$ and $5^\circ$ . . . . .	9
Variation with Mach number of the drag coefficient at zero lift and the longitudinal stability parameters for the recoverable booster alone. $\beta = 0^\circ$ . . . . .	10
Variation with Mach number of the aerodynamic-center location for the recoverable booster alone . . . . .	11





Figure

Variation of the lift-drag ratio with lift coefficient for the recoverable booster alone . . . . .	12
Variation with Mach number of $(L/D)_{\max}$ for the recoverable booster alone . . . . .	13
Effect of angle-of-attack variation with Mach number on the lateral-directional stability parameters for the recoverable booster alone . . . . .	14

DISCUSSION

Complete Launch Configuration

The normal-force contribution attributable to the winged spacecraft is shown by figure 4(a) to be insignificant over most of the angle-of-attack range despite the fact that the ratio of the spacecraft wing area to first-stage wing area is approximately 0.12. For example, the incremental normal-force coefficient at  $\alpha = 10^\circ$  for the spacecraft wing is less than 0.2, based on the total spacecraft wing area. Figure 4(c) and figure 6(b), however, show that the measured destabilizing contribution due to installation of the winged spacecraft is more than twice as much as can be calculated simply from the normal-force increment. Reference 1 indicates that significant interference effects in the form of reduced dynamic pressure were produced by the winged spacecraft and resulted in decreased stability contributions from the downstream booster fins. It may be concluded, therefore, that similar interference by the spacecraft wing on the normal-force distribution over the first-stage wing accounts at least partially for the anomalies indicated from the normal-force and pitching-moment curves. Figure 7 shows that the winged spacecraft caused a forward shift of about 20 percent in the center of pressure at  $\alpha = 0^\circ$  and that this shift was nearly constant with both Mach number and angle of attack. The magnitude of this center-of-pressure shift is significant if the same booster were to be used for a range of spacecraft types such as was tested here, since it may establish a requirement for both aerodynamic controls and rocket-engine gimbaling.

Figure 4(b) and figure 6(a) show that substitution of the winged spacecraft for the ballistic spacecraft caused an increase in the axial-force coefficient of about 0.004 at  $M = 0.6$ , but that at transonic speeds ( $0.98 < M < 1.20$ ) there is essentially no difference in the values at  $\alpha = 0^\circ$ . (For fig. 6(a) additional data at  $\alpha = 0^\circ$  have been added at  $M = 0.94$  and 1.02 to help to define the curve.) The difference in





the subsonic values probably results from a favorable interference on the axial force of the first-stage wing such as was reported in reference 1. Furthermore, there is probably an appreciable difference in the wave-drag contributions of the two spacecraft.

Lateral-directional stability for the launch configuration with the winged spacecraft is summarized in figure 8. The model is shown to be directionally stable up to an angle of attack of nearly  $10^\circ$ . Positive effective dihedral (negative  $C_{l_\beta}$ ) is shown for both angles of attack, and the usual increase in effective dihedral with angle of attack for highly swept wings is indicated. Although the significance of  $\frac{C_{l_\beta}}{C_{n_\beta}}$  for this type of vehicle is not known, it is observed that at

$\alpha = 0^\circ$  this ratio varies from about  $\frac{C_{l_\beta}}{C_{n_\beta}} = 1.0$  at  $M = 0.6$  to only about 0.2 at transonic speeds.

#### First-Stage Recoverable Booster

The first-stage recoverable booster was longitudinally stable throughout the Mach number and angle-of-attack ranges (figs. 9(c) and 10(c)) and shows only a moderate rate of increase in stability at transonic speeds. Failure to trim at positive angles of attack (fig. 9(c)), as would be expected for a configuration of this type, was apparently due to a small amount of warpage observed in the wing. The change in stability with Mach number is also shown in figure 11, in which the static margin increased from about 0.16c to 0.25c for the center-of-gravity location selected for reference. Although this 9-percent change is gradual, significant problems in longitudinal control may be encountered at hypersonic speeds.

The variation of the zero-lift drag coefficient with the base drag excluded (fig. 10(a)) is more nearly characteristic of cylindrical bodies with a blunt nose than of a wing-body combination. This behavior is probably attributable to the thin (only 2 percent) wing which produces little transonic wave drag as compared with the body itself. When the base drag is included, as would be the case for unpowered return flight, a substantial transonic drag rise is shown since the base pressure changes rapidly with Mach number at transonic speeds. For this model, the body base area was nearly 6 percent of the exposed wing area. The lift-drag ratios similarly reflect the inclusion of the base drag (fig. 12). The maximum lift-drag ratios (fig. 13) are shown to have been reduced from 8.8 to 7.5 at  $M = 0.6$  and from 5.4 to 4.6 at  $M = 1.2$ .

These reduced values of  $(L/D)_{\max}$  will have a degrading effect on the glide range and landing characteristics. Some alleviation may be obtained if boattailing is permitted by the rocket-nozzle shroud and/or if it is possible to vent the base to decrease the base drag. Alternatively, some low-speed thrust may be necessary to stretch the return range and provide, at the same time, possible "go-around" capability to improve landing reliability.

An appreciable increase in the effective dihedral occurred when the angle of attack was increased from  $0^\circ$  to  $10^\circ$  (fig. 14(a)), but the variation with Mach number was small. The directional stability did not deteriorate appreciably with angle of attack (fig. 14(b)). The relatively large value of the directional-stability parameter, coupled with small effective dihedral at low angles of attack, may cause some spiral instability at  $M = 0.6$ . The ratio of roll to yaw at  $\alpha = 0^\circ$  is  $\frac{C_{l\beta}}{C_{n\beta}} \approx 0.2$ , but this ratio increases to about 1.3 at  $\alpha = 10^\circ$ . Since no

Dutch roll would be anticipated from these ratios, the autopilot can probably overcome the poor spiral stability at low angles of attack. Although the relatively large vertical tail used for these tests (vertical-tail area was 12.5 percent of wing area) provided more than adequate transonic directional stability, this much vertical-tail area is believed to be necessary to achieve sufficient directional stability at supersonic speeds.

#### CONCLUDING REMARKS

An investigation has been made of a model of a preliminary three-stage launch configuration with a horizontal-landing recoverable booster in the Langley 8-foot transonic pressure tunnel. The stability of both the launch vehicle, with either a ballistic spacecraft or a winged spacecraft, and the recoverable booster alone was determined over a Mach number range from 0.6 to 1.2 and at angles of attack up to  $14^\circ$ . The principal results were as follows:

1. The winged spacecraft was responsible for a significant destabilizing increment which could not be accounted for simply by the normal-force increments due to the spacecraft wing, but which must be due in part to interference on the wing of the first-stage recoverable booster.

2. The nearly 20-percent shift in the center of pressure caused by the winged spacecraft may require use of aerodynamic controls as well as engine gimbaling if the same booster is to be used for both ballistic and winged spacecraft.

3. The recoverable booster alone was stable both longitudinally and laterally; however, some spiral instability at low angles of attack may exist.

4. The high base drag for the recoverable stage alone corresponding to power-off return indicates a probable need for boattailing or venting of the base to improve low-speed lift-drag ratios.

Langley Research Center,  
National Aeronautics and Space Administration,  
Langley Station, Hampton, Va., March 16, 1962.

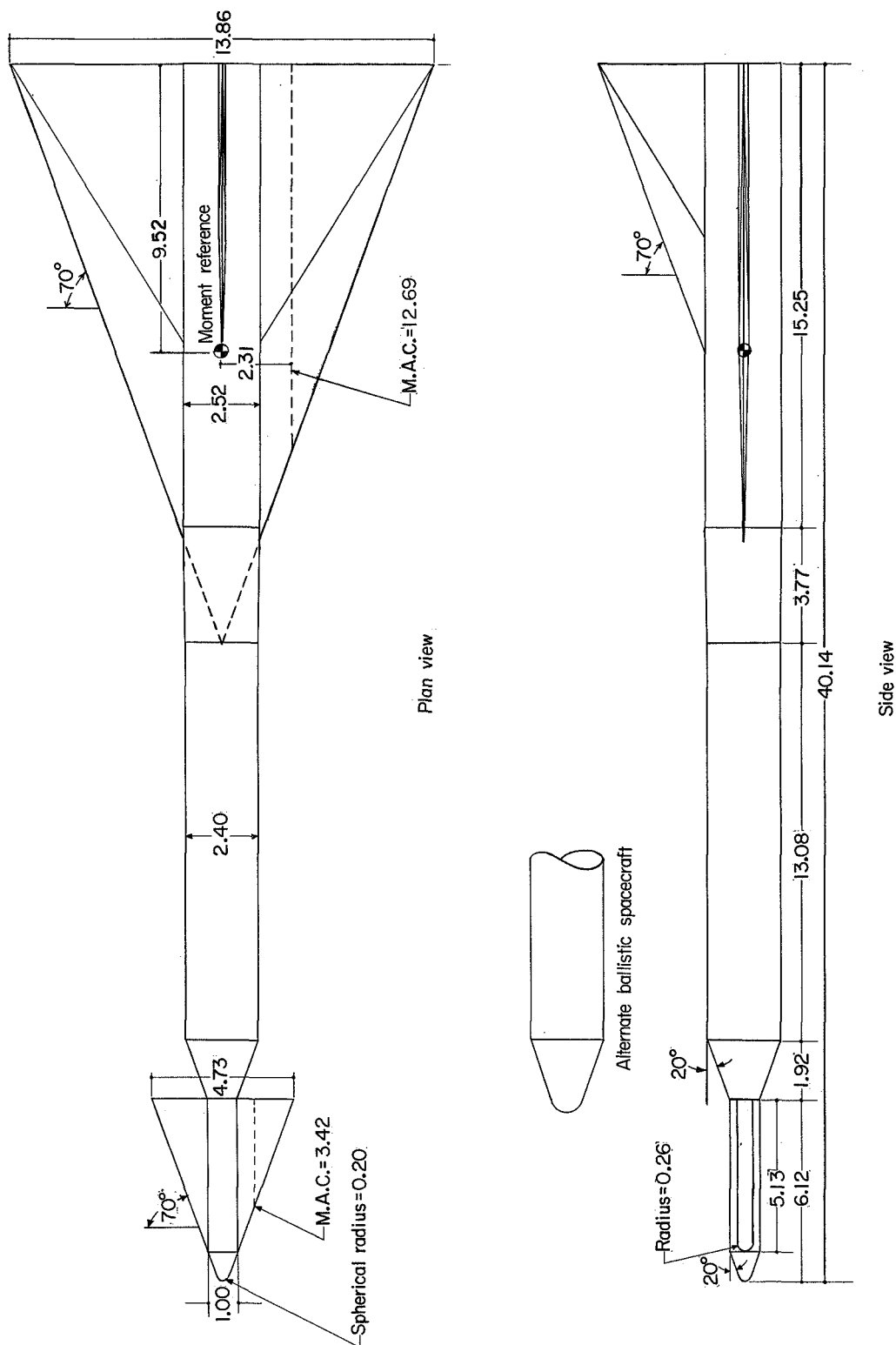
L  
1  
9  
3  
4

#### REFERENCE

1. Pierpont, P. Kenneth: Preliminary Investigation of Interference Effects of Multicoplanar Fins on a Two-Stage Rocket Launch Vehicle With Winged Spacecraft at Transonic Speeds. NASA TM X-677, 1962.

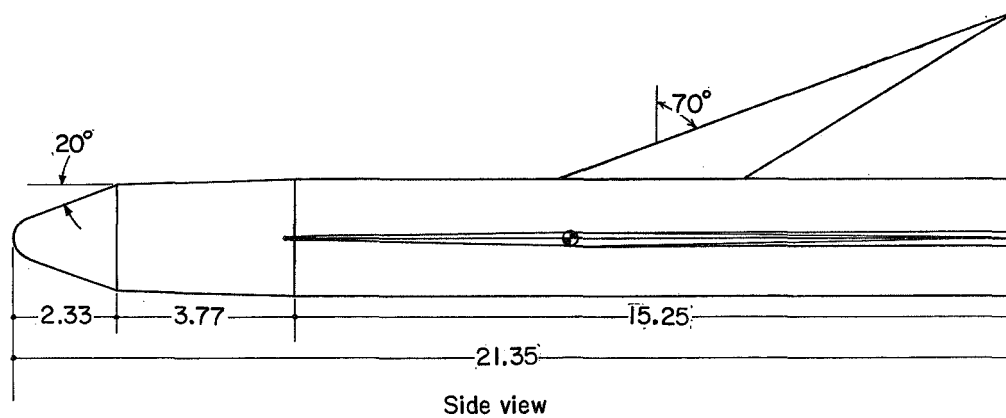
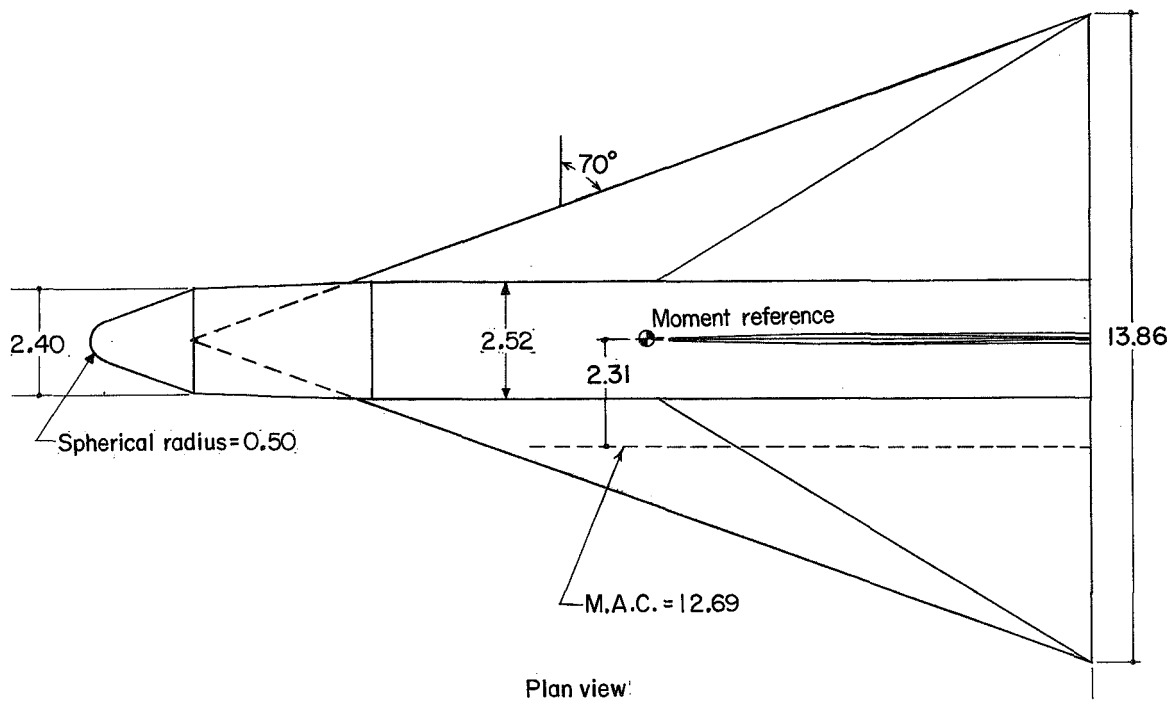
TABLE I.- GEOMETRIC CHARACTERISTICS OF MODEL

Recoverable-booster stage:	
Length including interstage and nose cone, in. . . . .	21.35
Diameter, in. . . . .	2.52
Cross-sectional area, sq in. . . . .	4.99
Length-diameter ratio . . . . .	8.5
Wing:	
Area, total, sq in. . . . .	132
Area, exposed, sq in. . . . .	88.3
Span, total, in. . . . .	13.86
Root chord, in. . . . .	19.05
Tip chord . . . . .	0.00
Leading-edge sweep angle, deg . . . . .	70
Thickness ratio . . . . .	0.02
Leading-edge radius, in. . . . .	0.007
Position of maximum thickness, percent chord . . . . .	40
Mean aerodynamic chord (total area), in. . . . .	12.69
Moment reference center, percent M.A.C. . . . .	25
Moment reference center, in. from base . . . . .	9.52
Vertical fin:	
Area, sq in. . . . .	16.43
Root chord, in. . . . .	9.50
Thickness ratio . . . . .	0.02
Span, in. . . . .	3.46
Leading-edge sweep angle, deg . . . . .	70
Leading-edge radius, in. . . . .	0.004
Second-stage expendable rocket booster:	
Length, in. . . . .	13.08
Diameter, in. . . . .	2.40
Length-diameter ratio . . . . .	5.5
Third-stage, ballistic spacecraft:	
Diameter, in. . . . .	2.40
Nose-cone included angle, deg . . . . .	40
Length, in. . . . .	2.33
Nose radius, in. . . . .	0.50
Third-stage, winged spacecraft:	
Body diameter, in. . . . .	1.0
Body length, including interstage, in. . . . .	8.04
Nose-cone included angle, deg . . . . .	40
Nose radius, in. . . . .	0.20
Wing area, total, sq in. . . . .	15.38
Wing area, exposed, sq in. . . . .	9.57
Wing span, in. . . . .	4.73
Thickness ratio . . . . .	0.10
Leading-edge radius (root), in. . . . .	0.26
Root chord, in. . . . .	6.50
Tip chord, in. . . . .	0
Leading-edge sweep angle, deg . . . . .	70
M.A.C. of exposed area, in. . . . .	3.42
Moment arm measured from center of gravity to 0.25 M.A.C. of third-stage wing, in. . . . .	29.16



(a) Complete model shown with winged spacecraft.

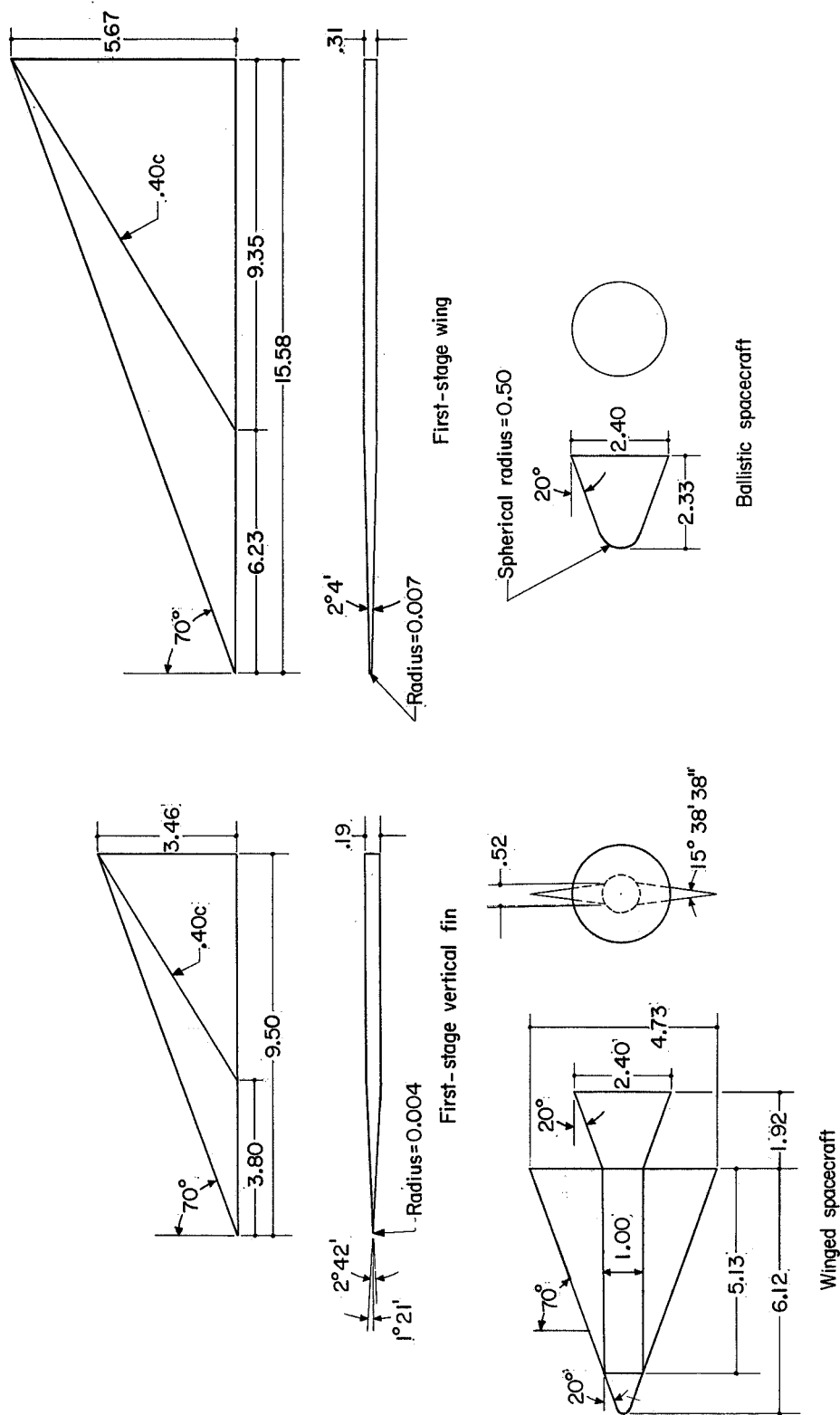
Figure 1.- Model details and dimensions. All linear dimensions are in inches.



(b) Recoverable first stage.

Figure 1.- Continued.

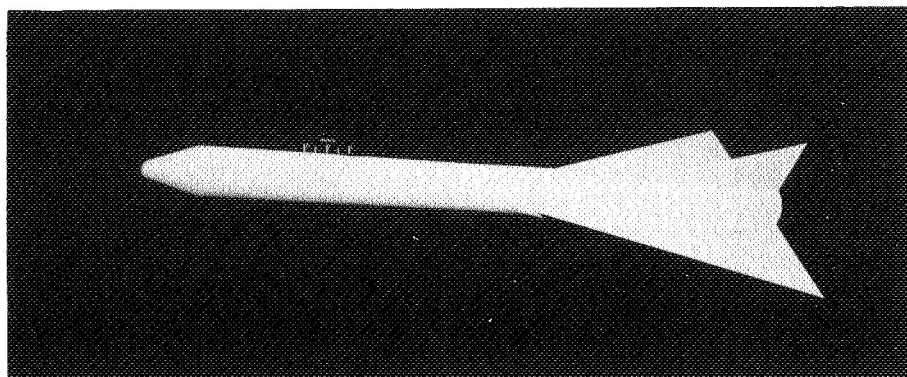
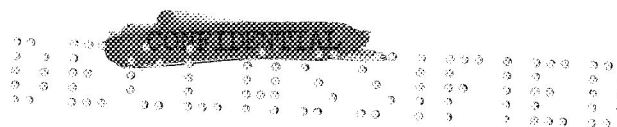




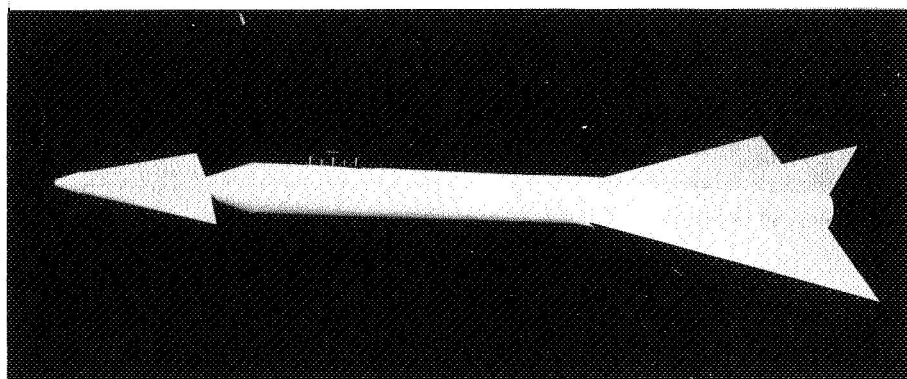
(c) Details of aerodynamic surfaces and spacecraft.

Figure 1.- Concluded.

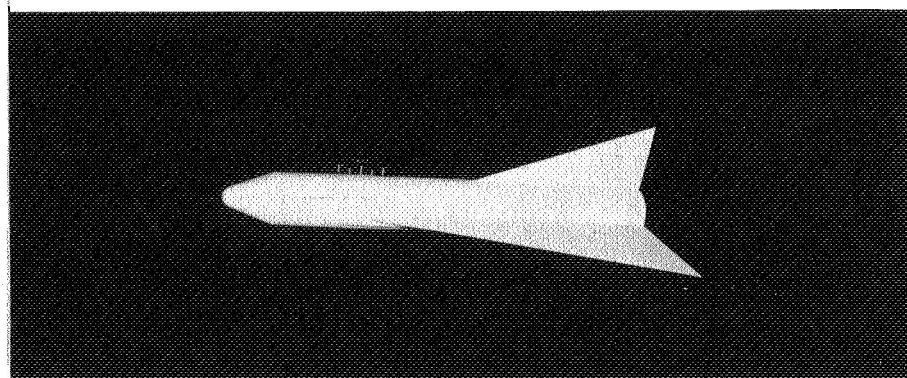




(a) Launch configuration with ballistic nose cone. L-61-7509



(b) Launch configuration with winged spacecraft. L-61-7511



(c) Recoverable stage of launch vehicle. L-61-7512

Figure 2.- Photographs of models.



L-1934

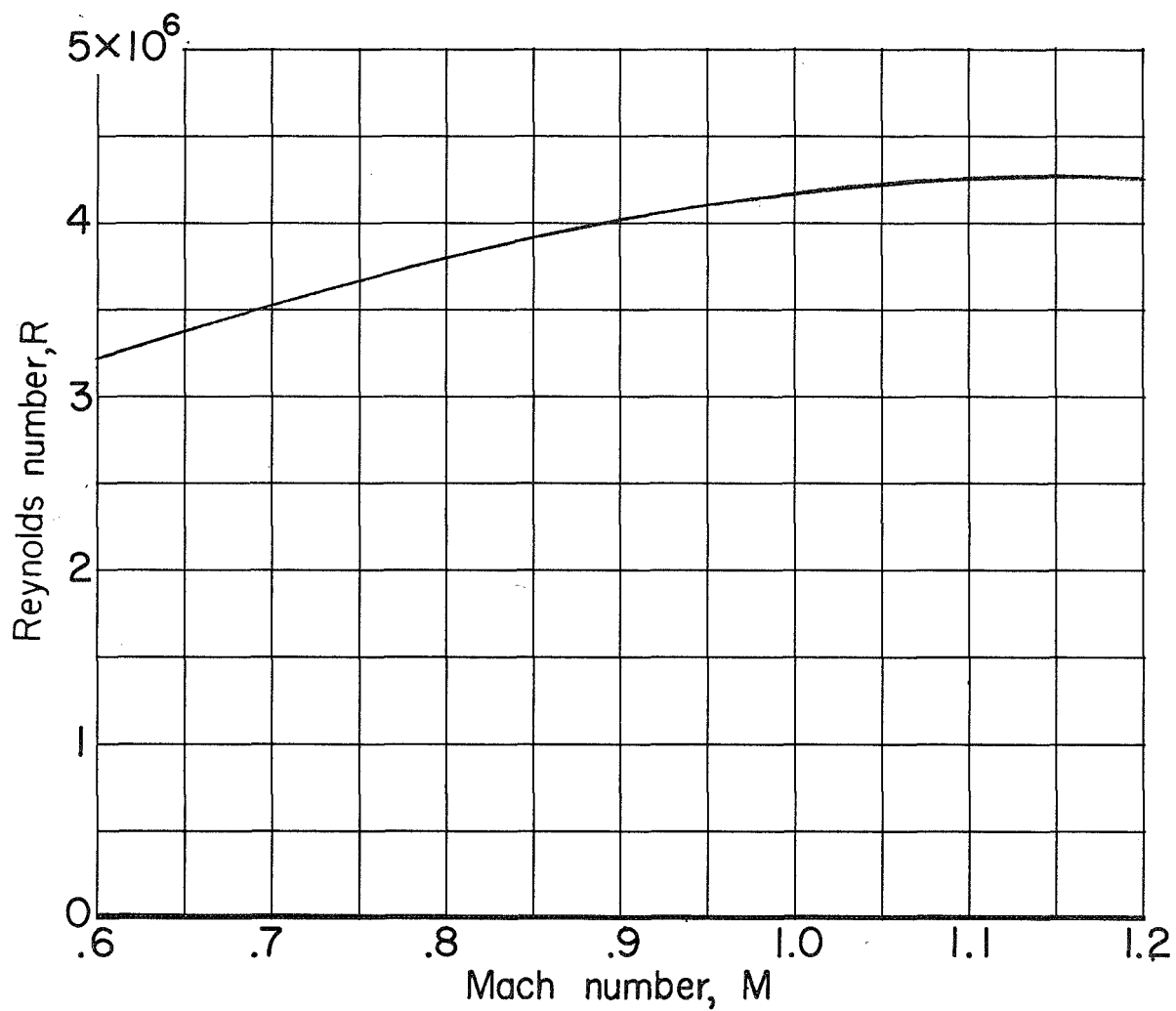
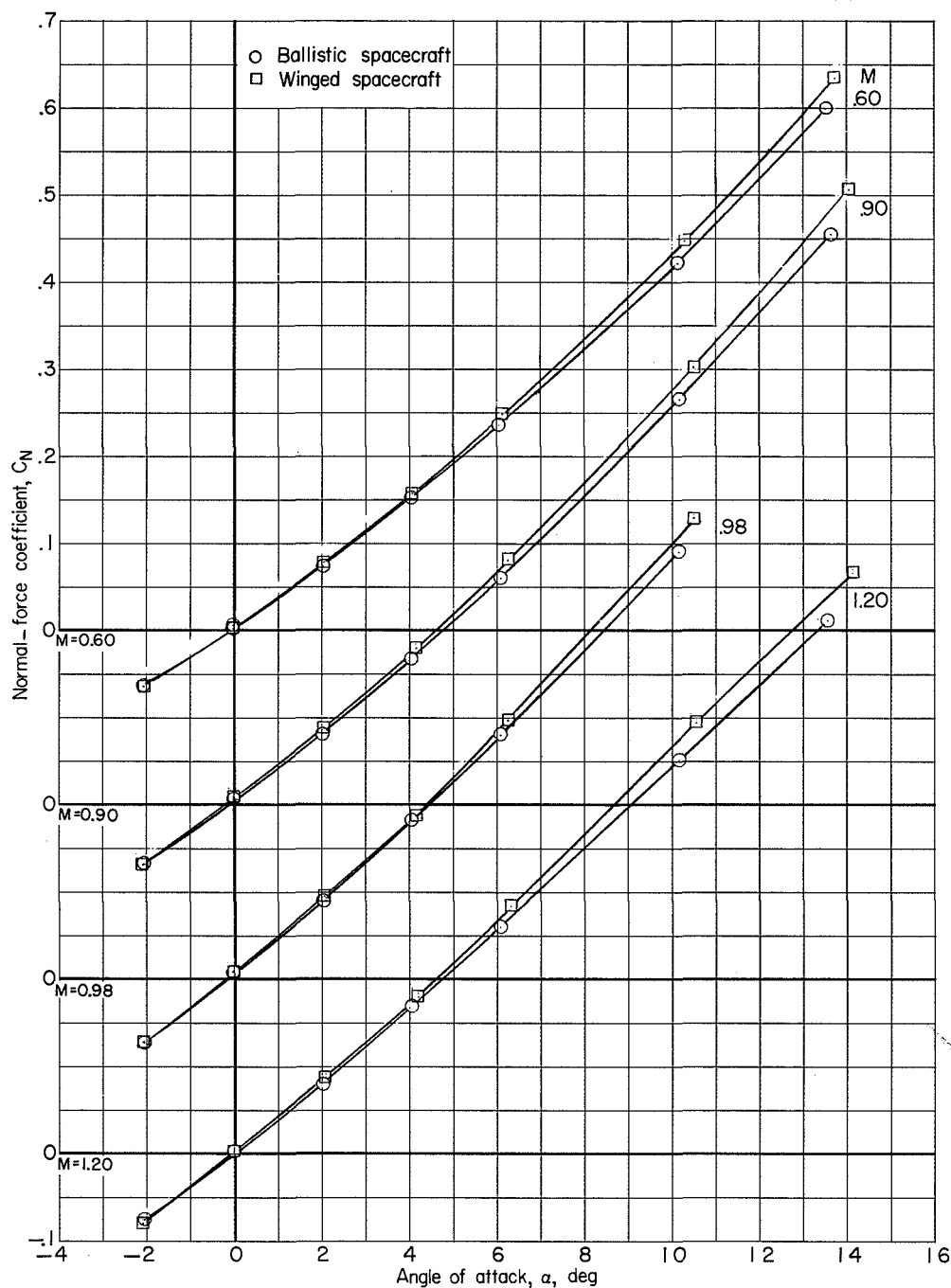
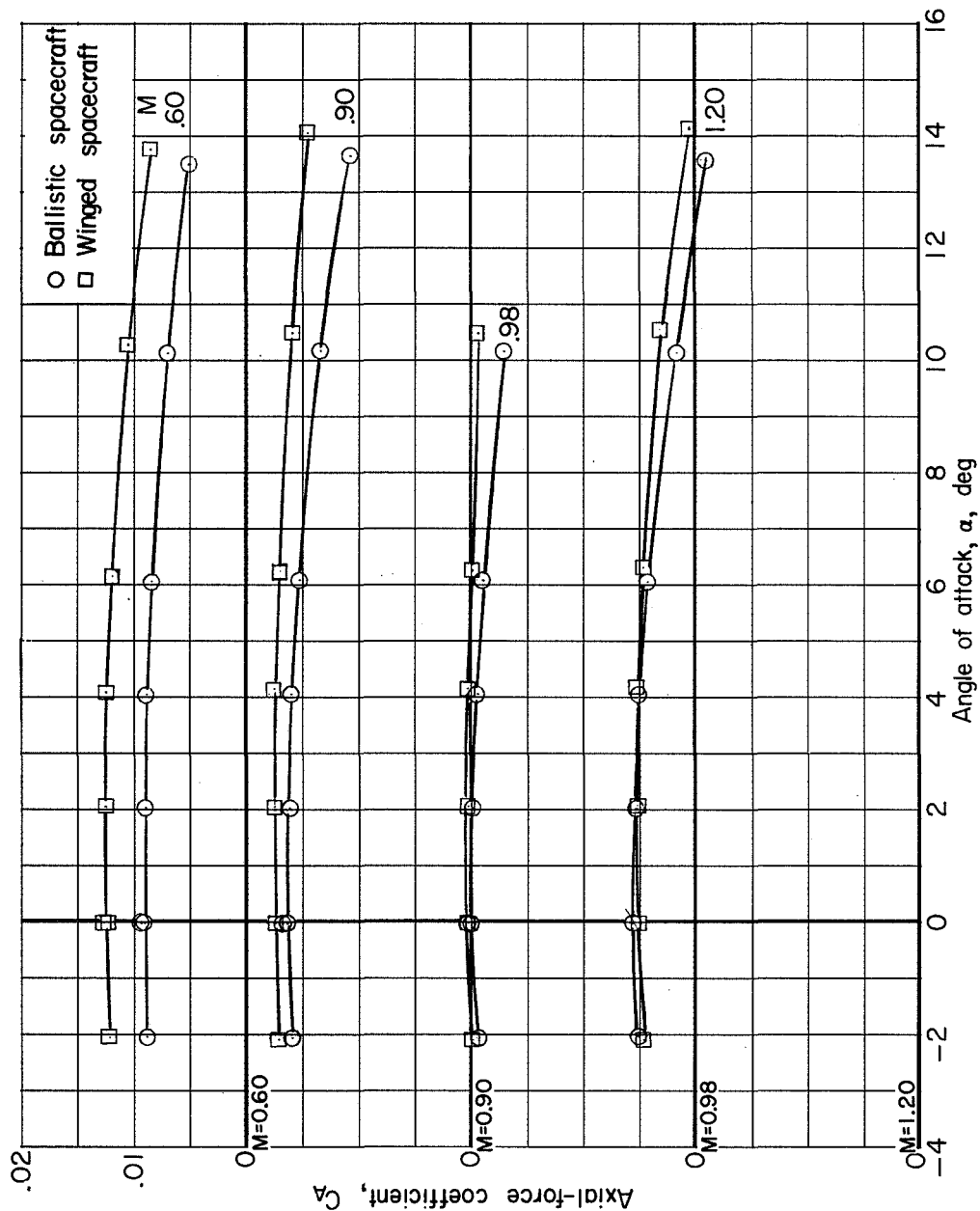


Figure 3.- Variation with Mach number of the test Reynolds number per foot.



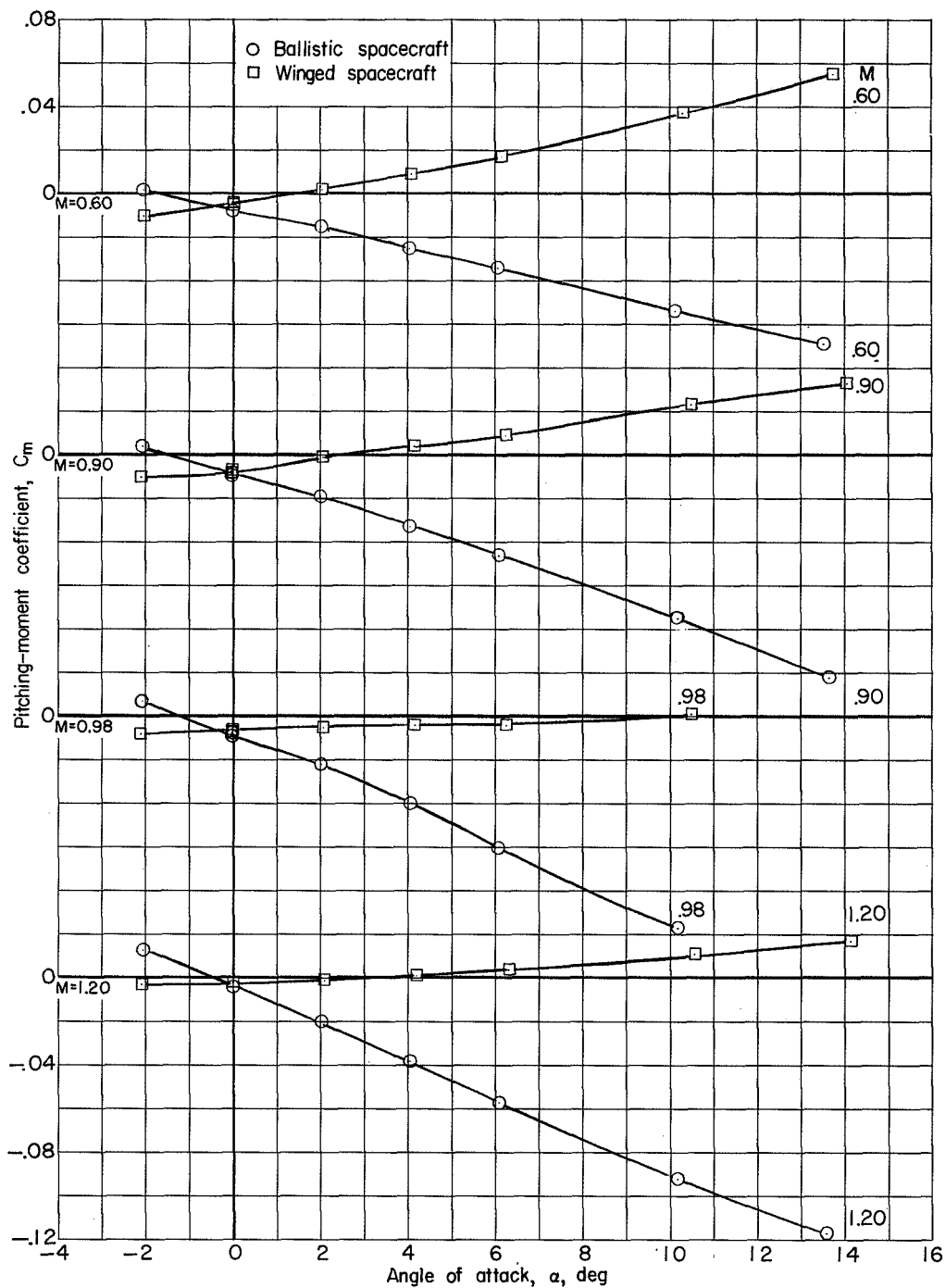
(a) Normal-force coefficient plotted against angle of attack.

Figure 4.- Longitudinal aerodynamic characteristics of the launch vehicle with a ballistic and a winged spacecraft.  $\beta = 0^\circ$ .



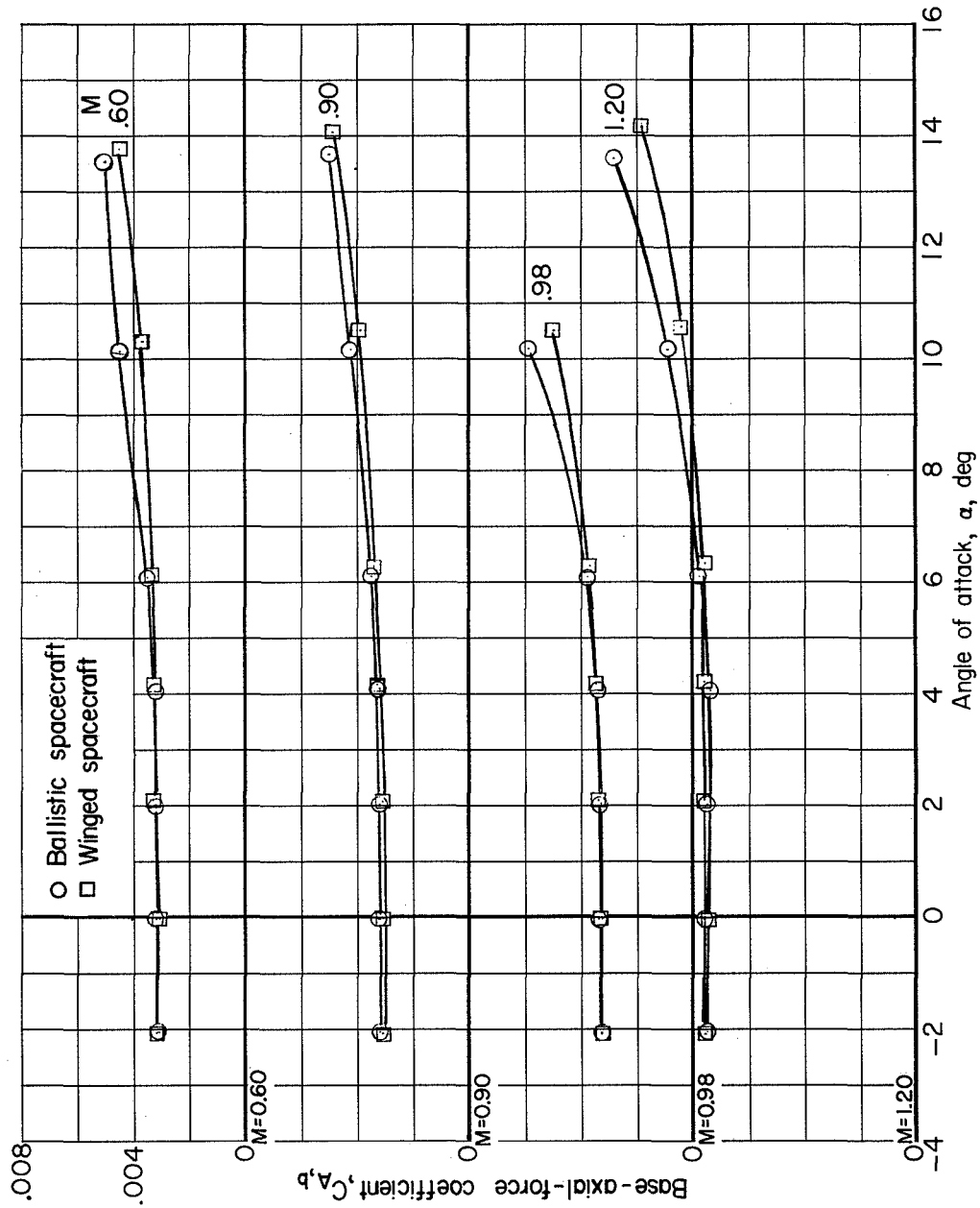
(b) Axial-force coefficient plotted against angle of attack.

Figure 4.- Continued.



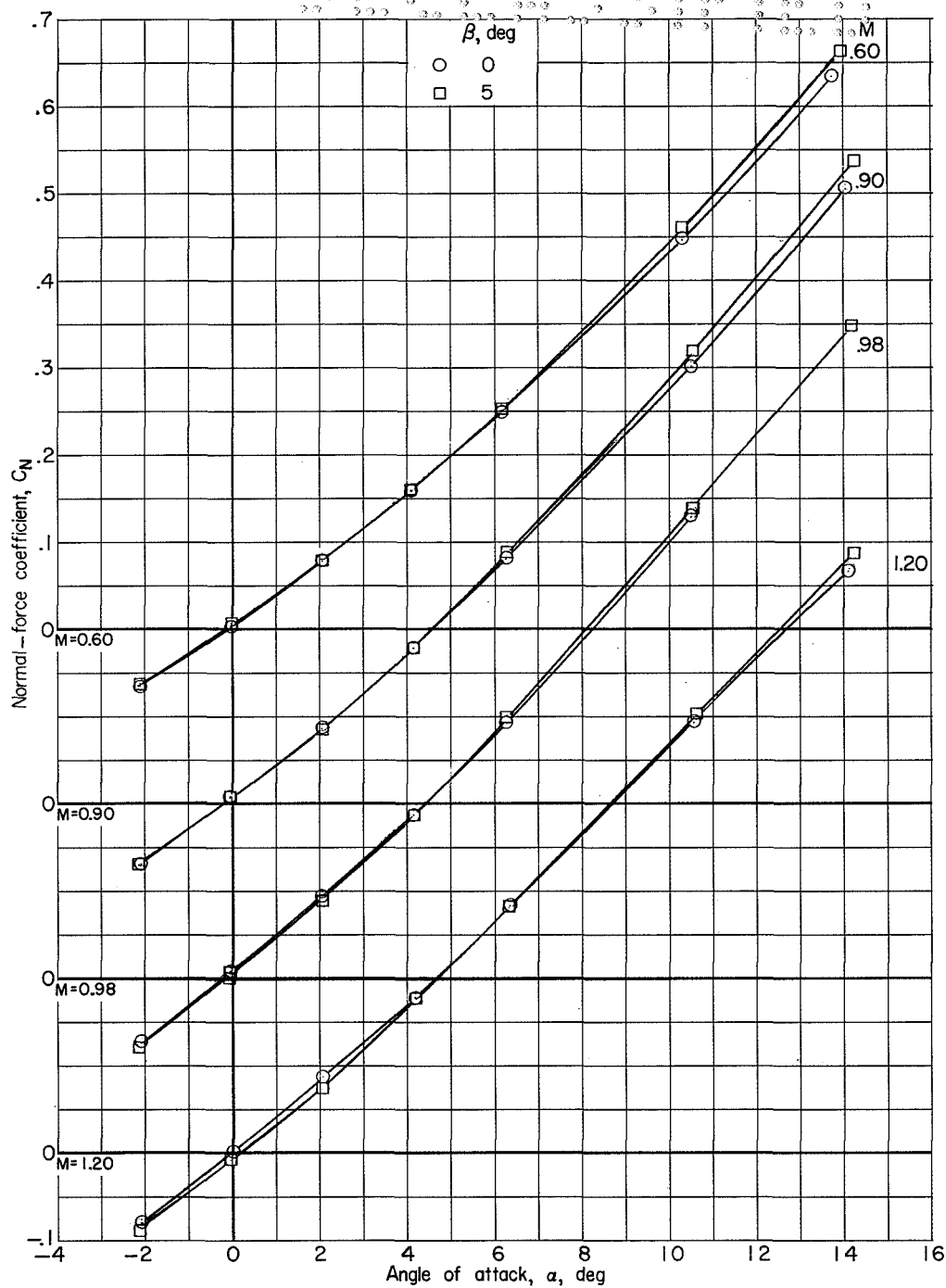
(c) Pitching-moment coefficient plotted against angle of attack.

Figure 4.- Continued.



(d) Base-axial-force coefficient plotted against angle of attack.

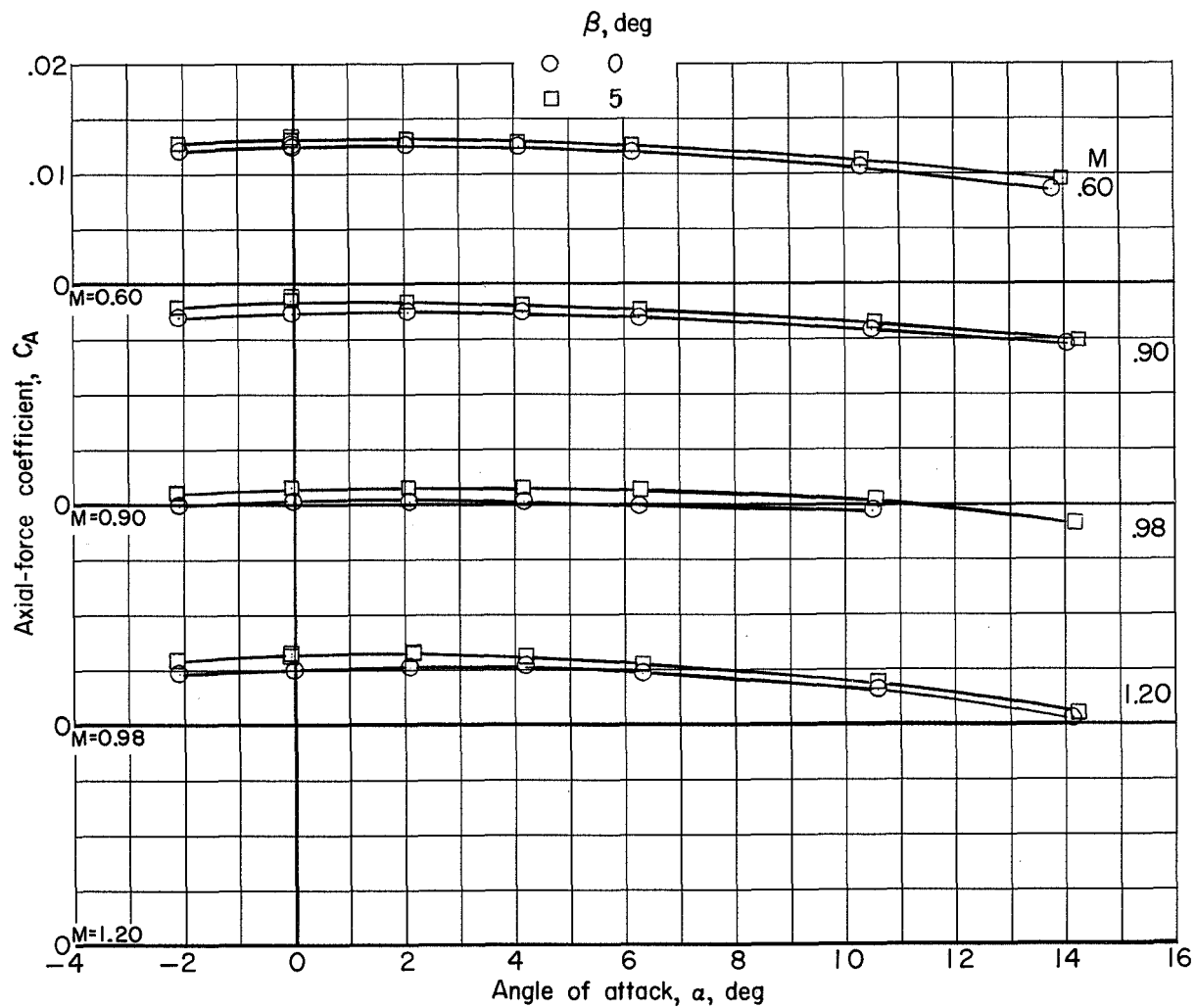
Figure 4.- Concluded.



(a) Normal-force coefficient plotted against angle of attack.

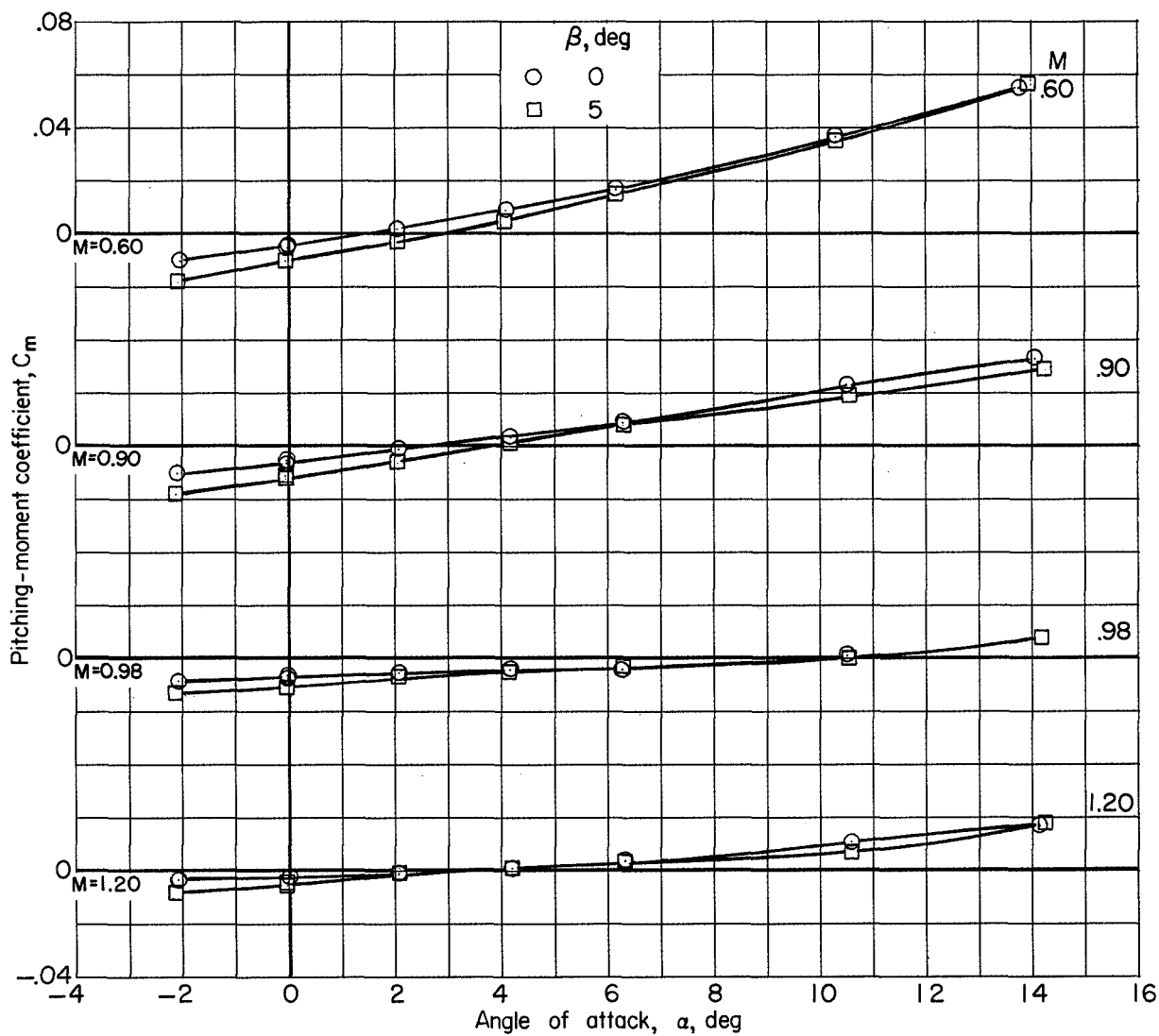
Figure 5.- Aerodynamic characteristics of the launch vehicle with winged spacecraft.  $\beta = 0^\circ$  and  $5^\circ$ .





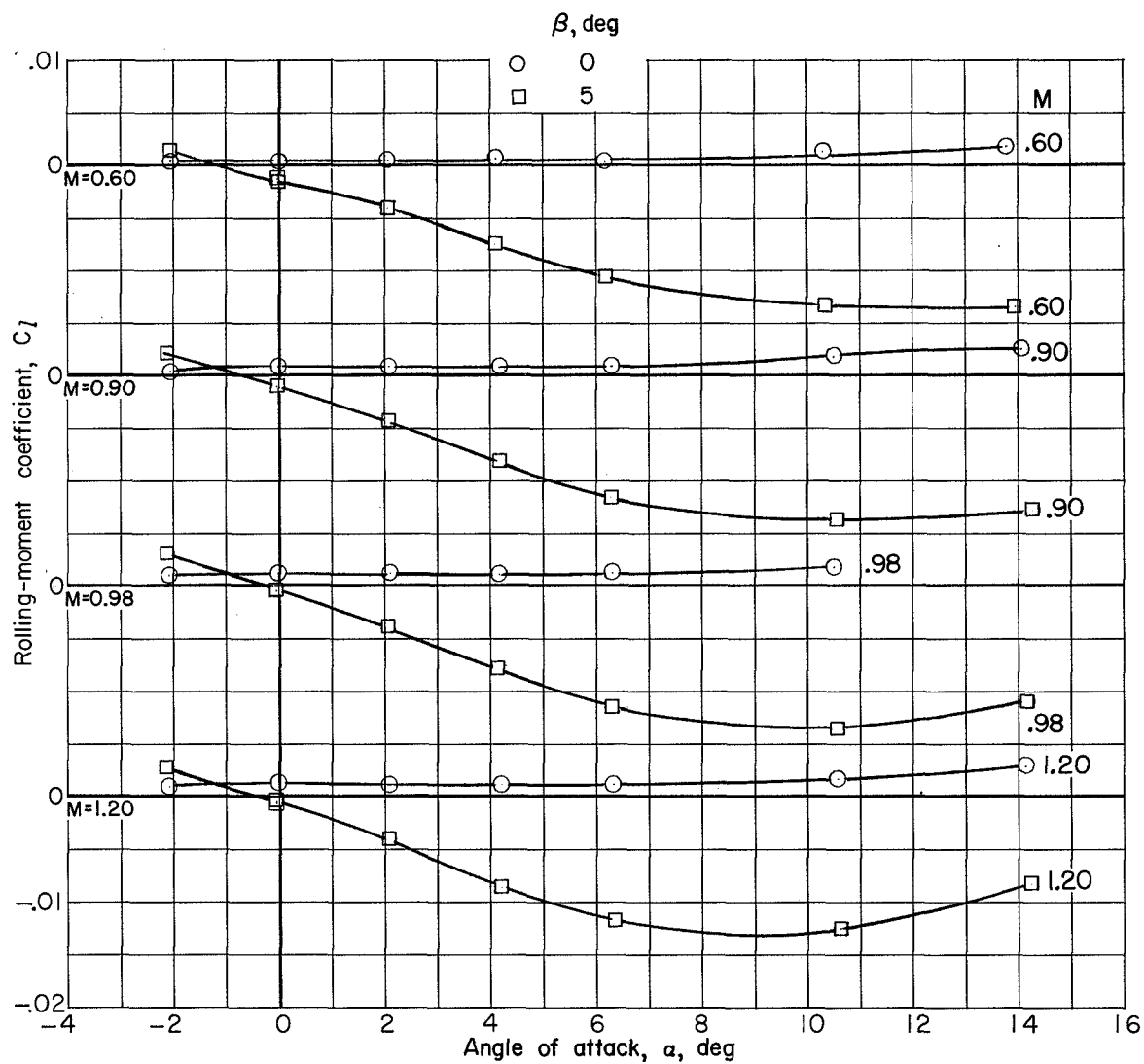
(b) Axial-force coefficient plotted against angle of attack.

Figure 5.- Continued.



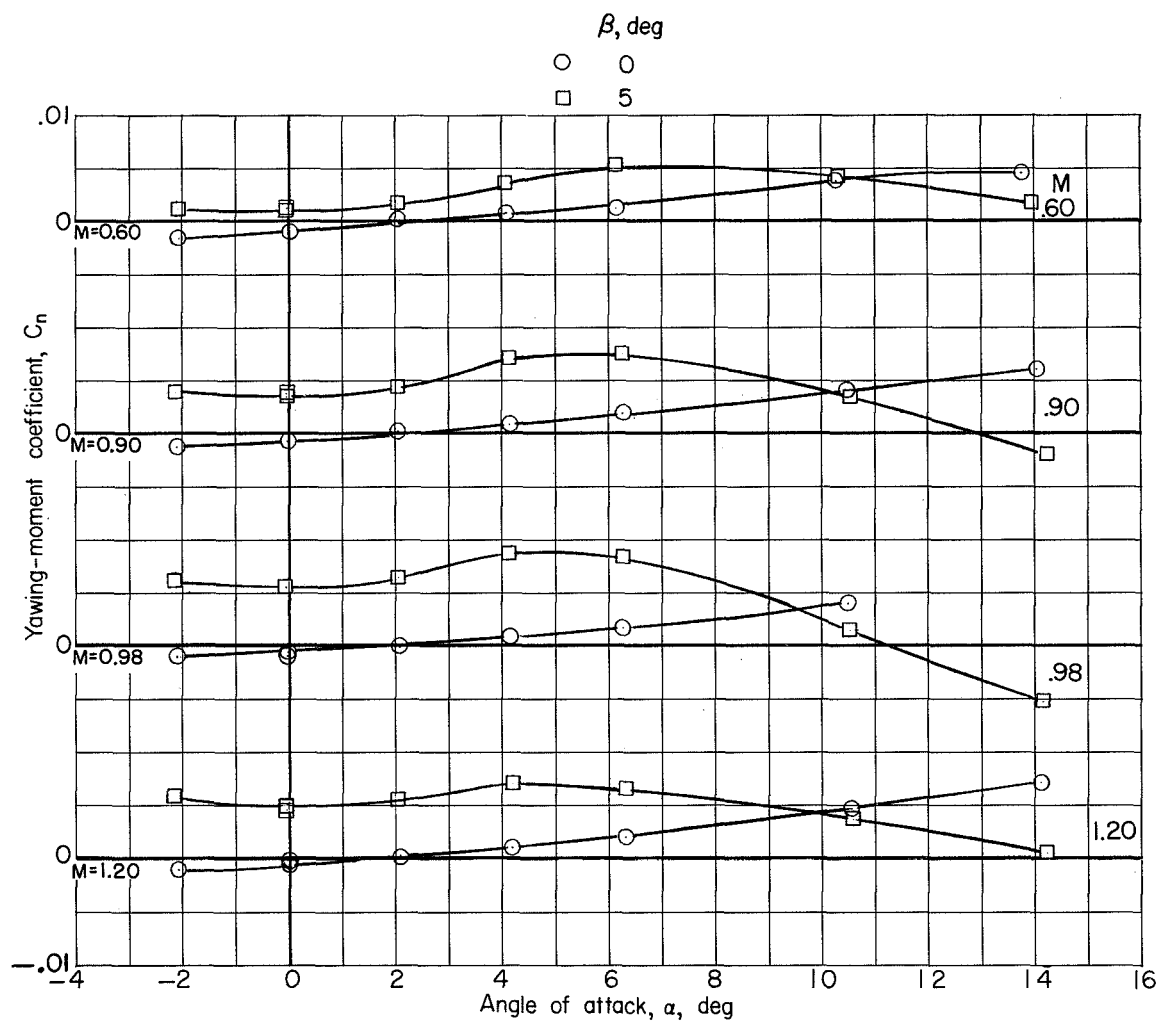
(c) Pitching-moment coefficient plotted against angle of attack.

Figure 5.- Continued.



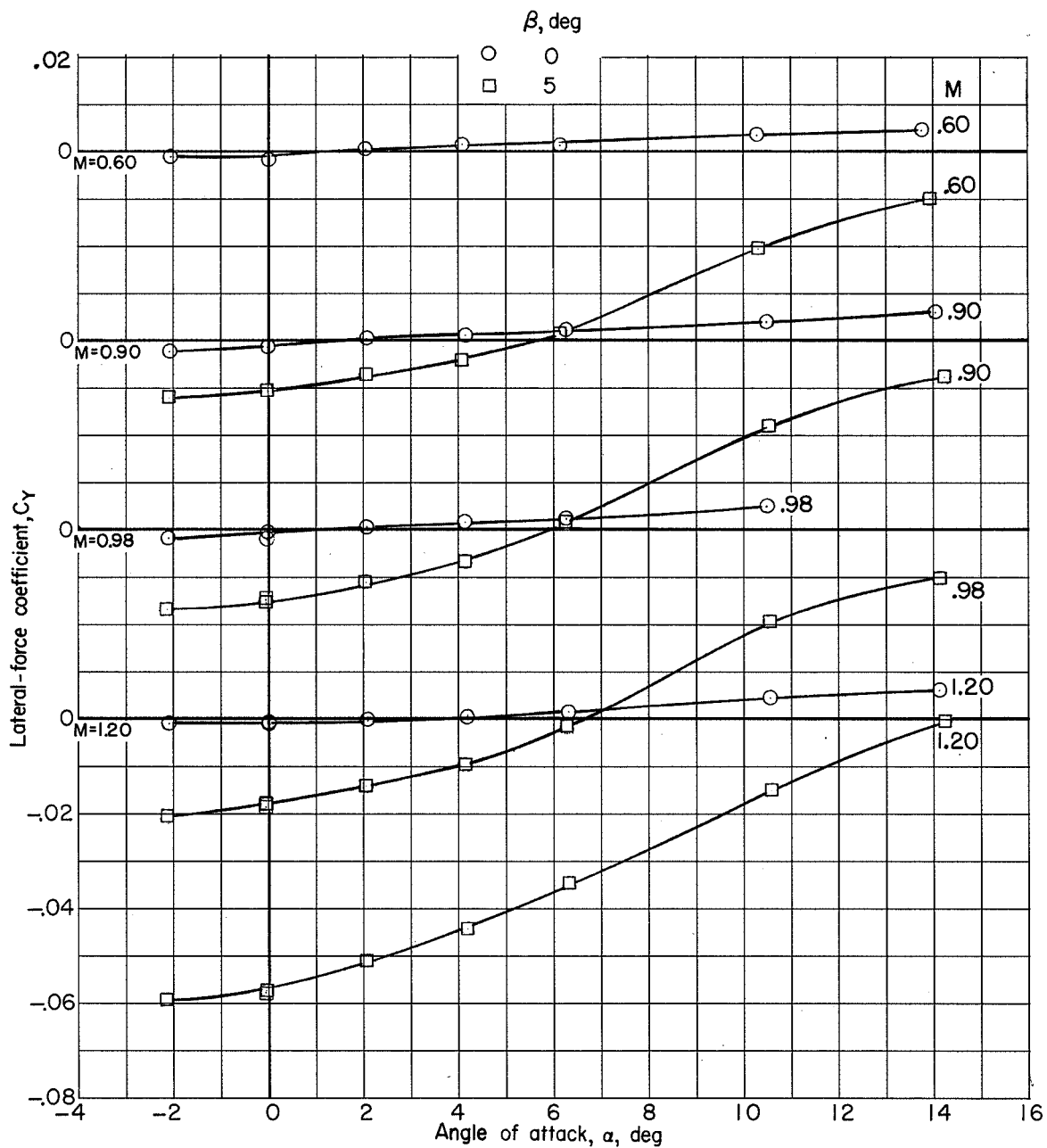
(d) Rolling-moment coefficient plotted against angle of attack.

Figure 5.- Continued.



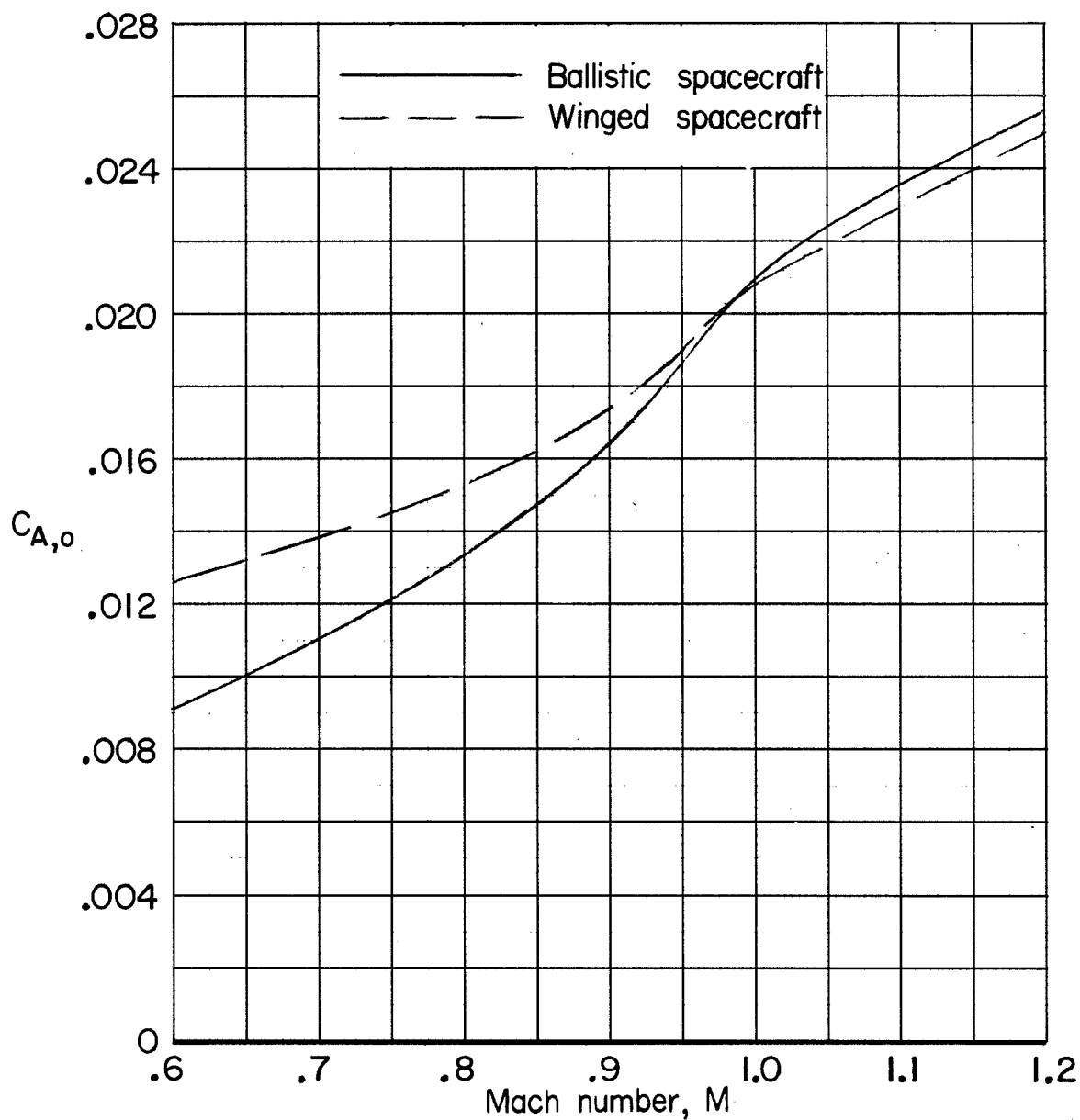
(e) Yawing-moment coefficient plotted against angle of attack.

Figure 5.- Continued.



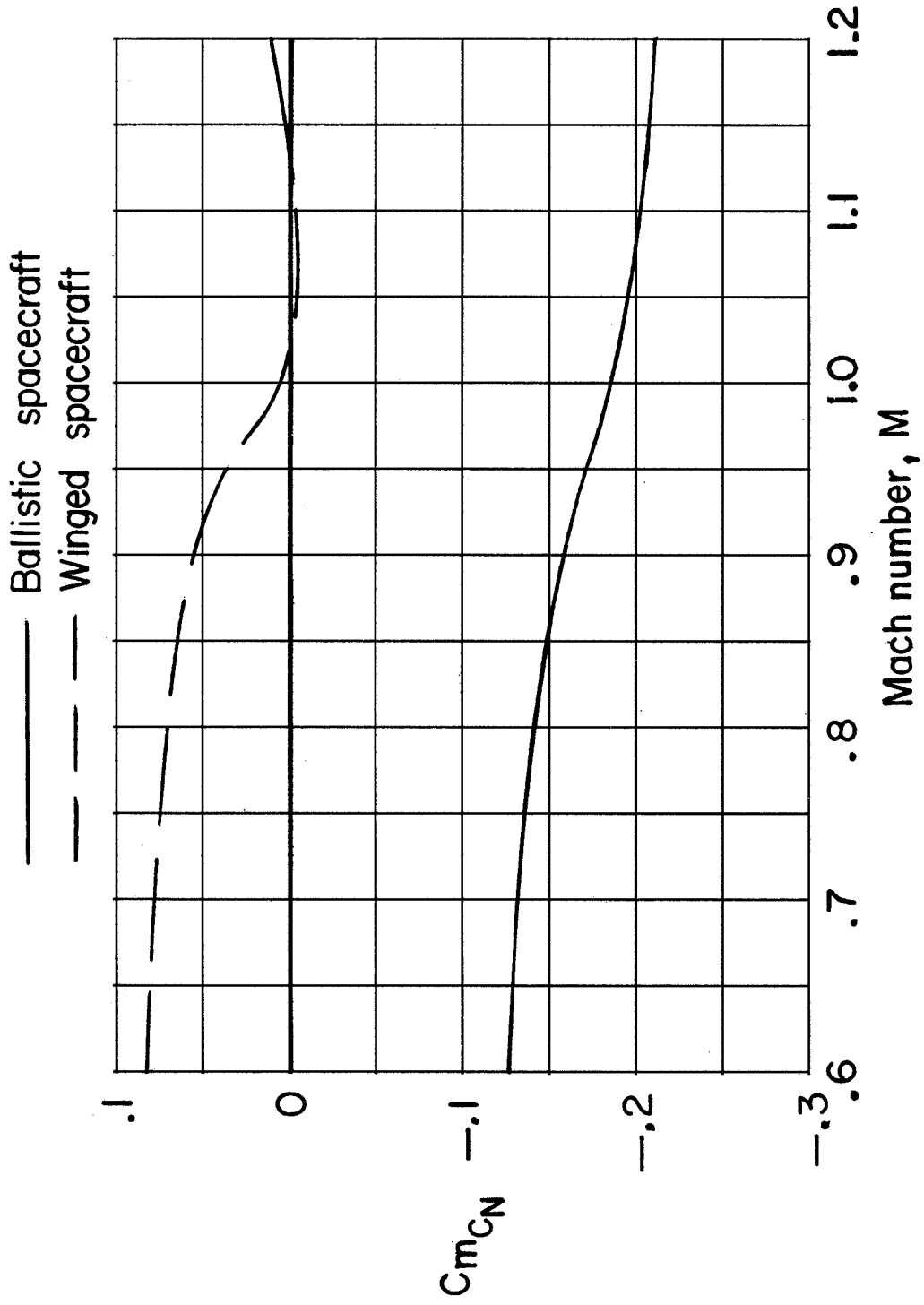
(f) Lateral-force coefficient plotted against angle of attack.

Figure 5.- Concluded.



(a) Axial-force coefficient.

Figure 6.- Variation of the axial-force coefficient and longitudinal stability parameter for the launch vehicle with ballistic and winged spacecraft.  $\alpha = 0^\circ$ .



(b) Longitudinal stability parameter.

Figure 6.- Concluded.



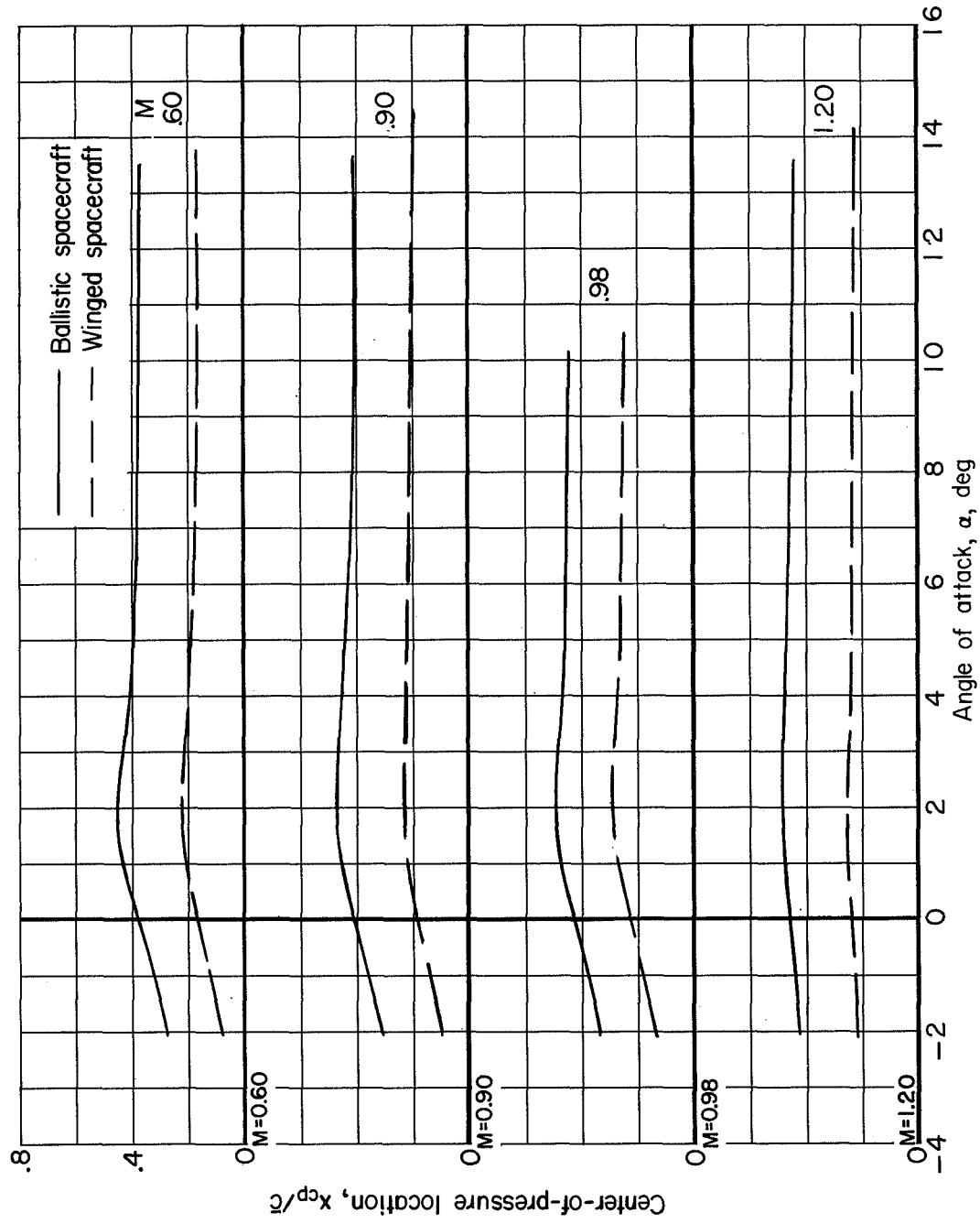
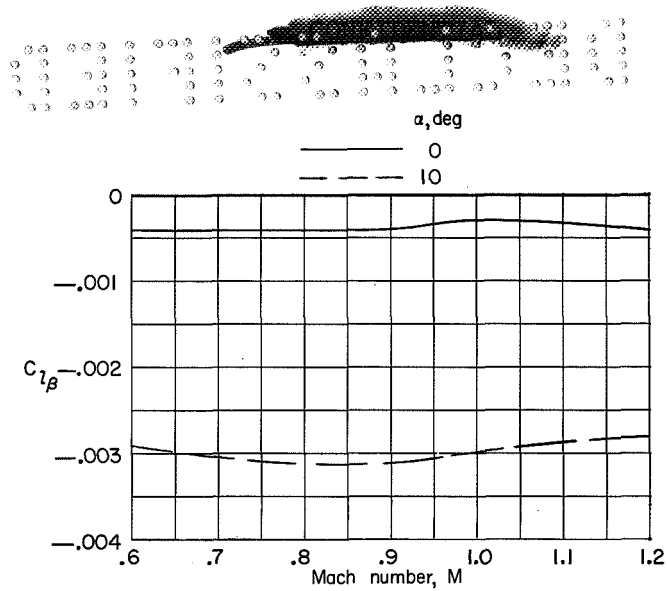
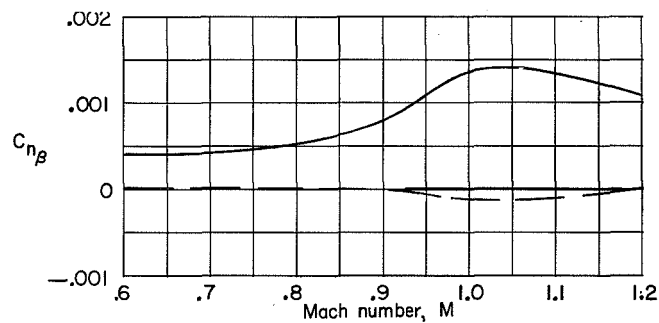


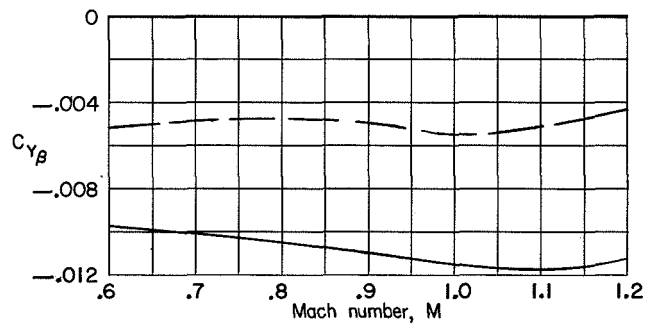
Figure 7.- Variation of the center-of-pressure location with angle of attack for the launch vehicle with ballistic and winged spacecraft.



(a) Effective dihedral parameter plotted against Mach number.

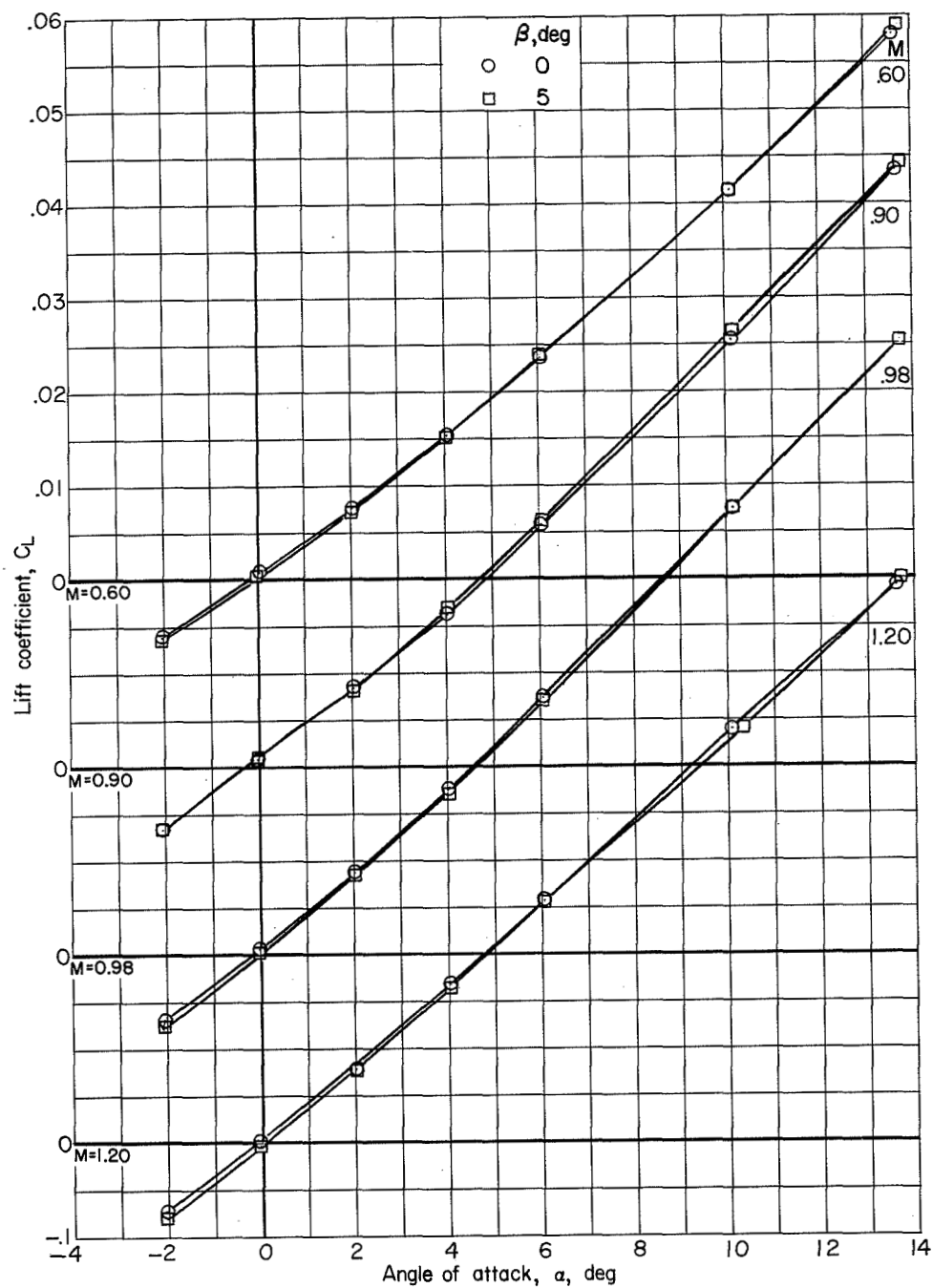


(b) Directional stability parameter plotted against Mach number.



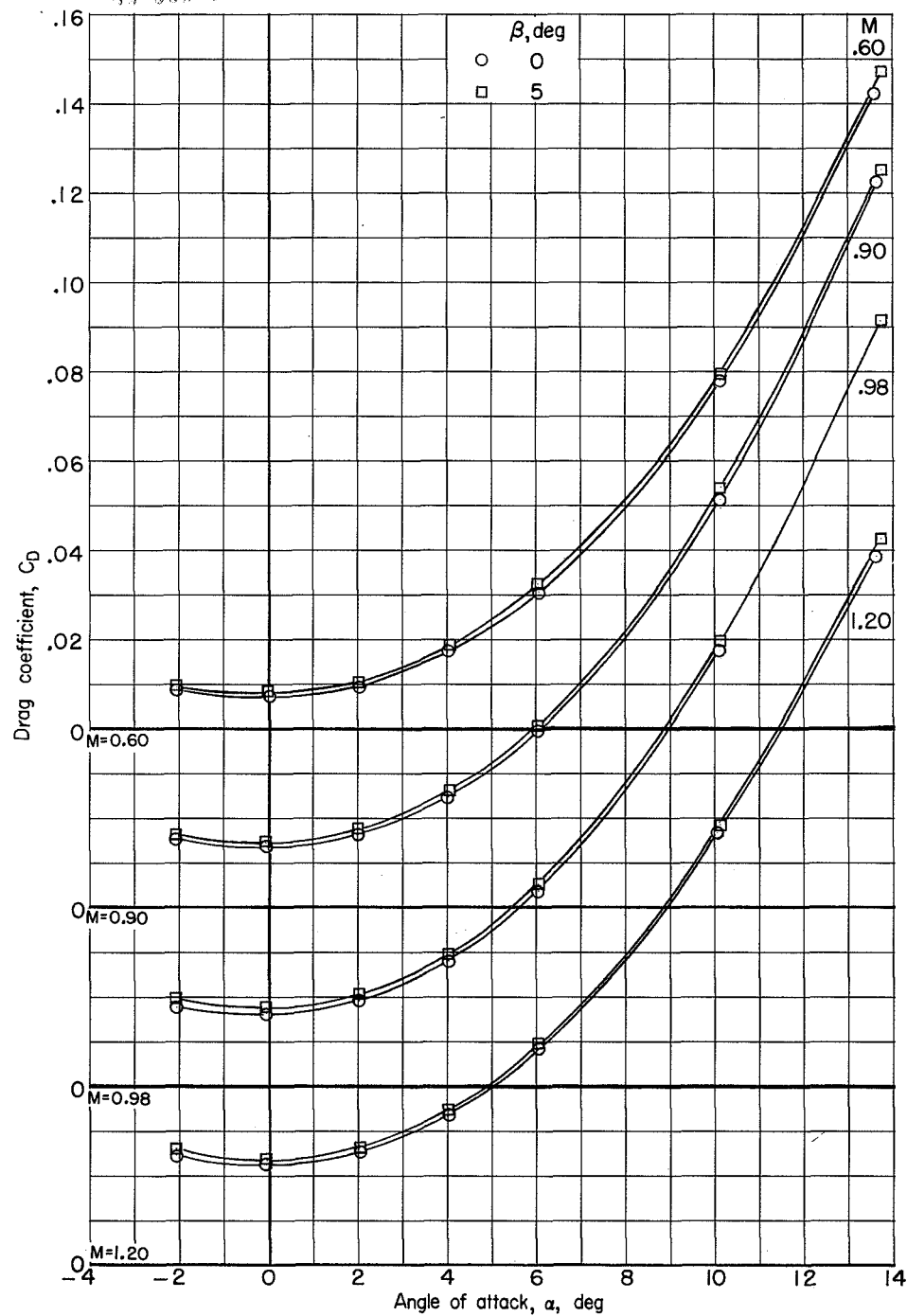
(c) Lateral-force parameter plotted against Mach number.

Figure 8.- Effect of angle of attack on the variation of the lateral-directional stability parameters with Mach number for the launch vehicle with winged spacecraft.



(a) Lift coefficient plotted against angle of attack.

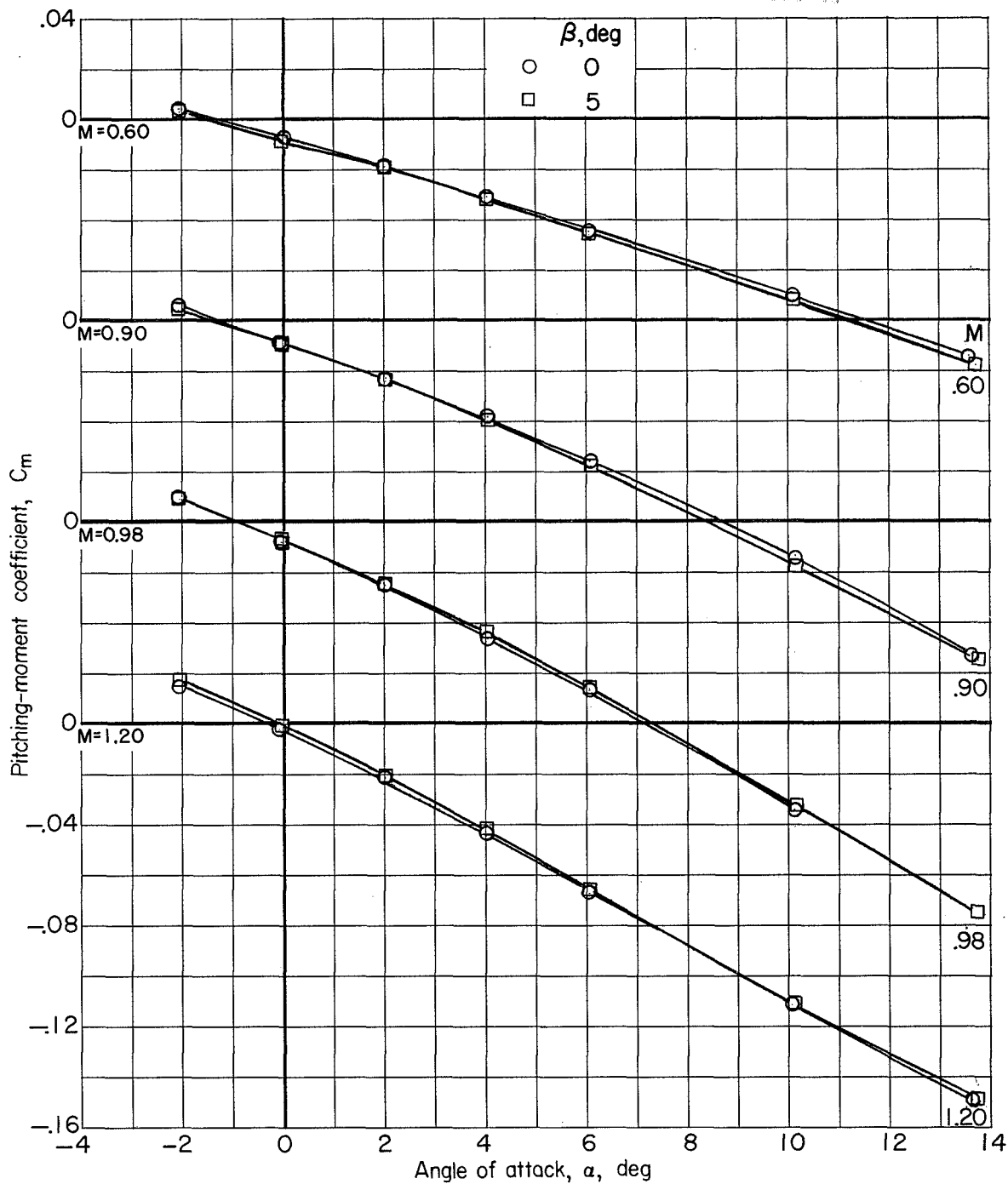
Figure 9.- Aerodynamic characteristics of the recoverable booster alone at  $\beta = 0^\circ$  and  $5^\circ$ .



(b) Drag coefficient plotted against angle of attack.

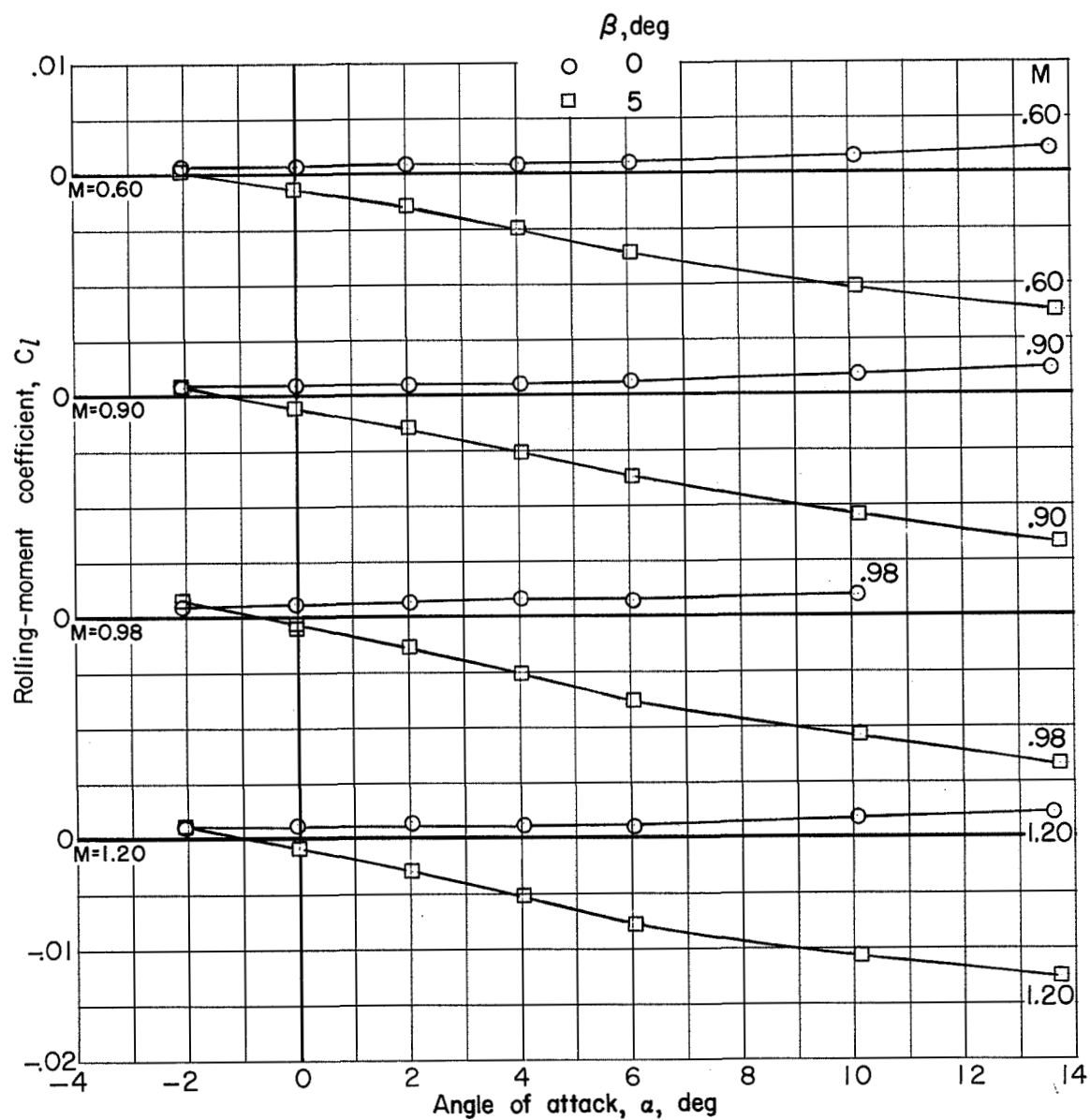
Figure 9.- Continued.

L-1934



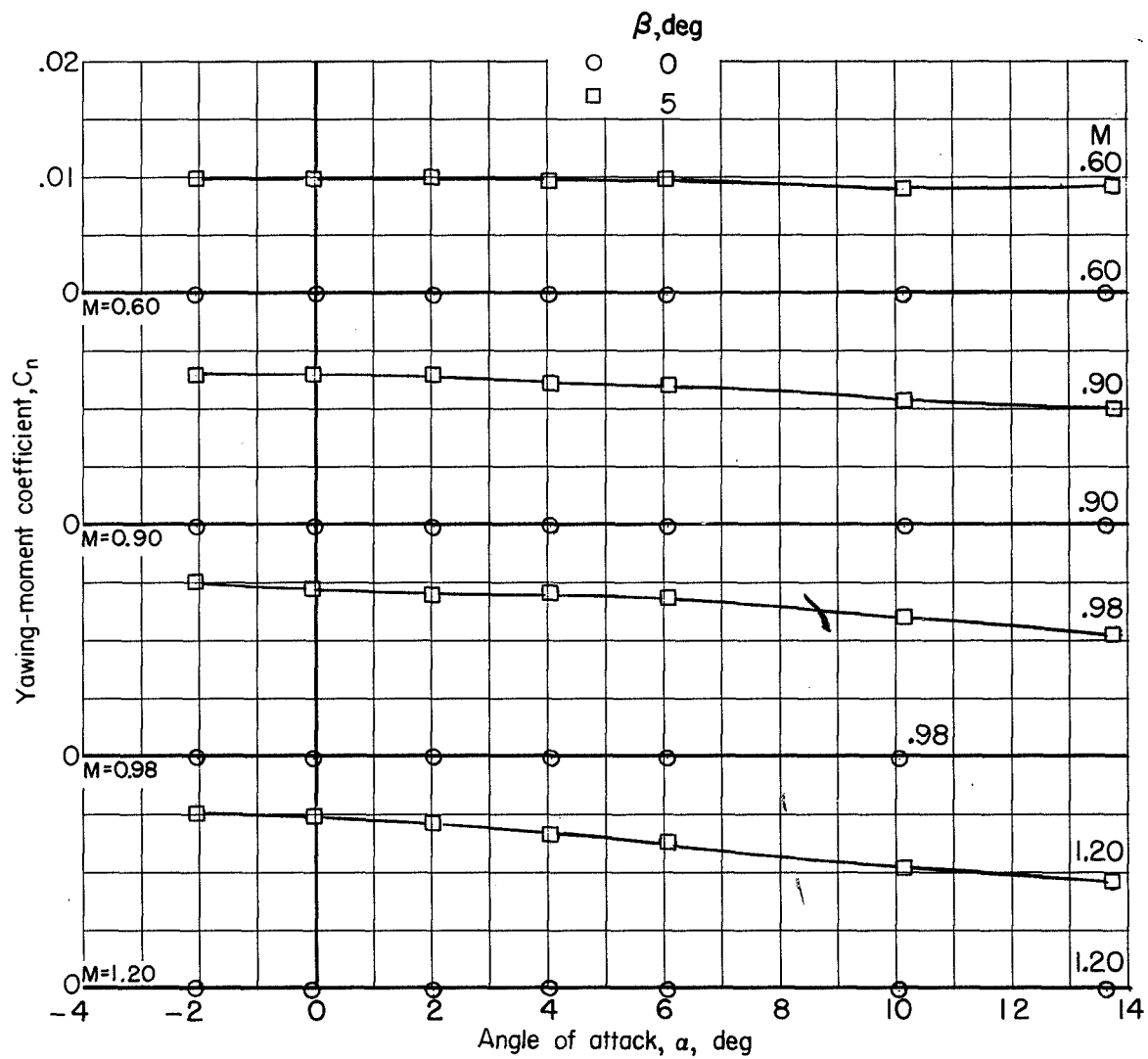
(c) Pitching-moment coefficient plotted against angle of attack.

Figure 9.- Continued.



(d) Rolling-moment coefficient plotted against angle of attack.

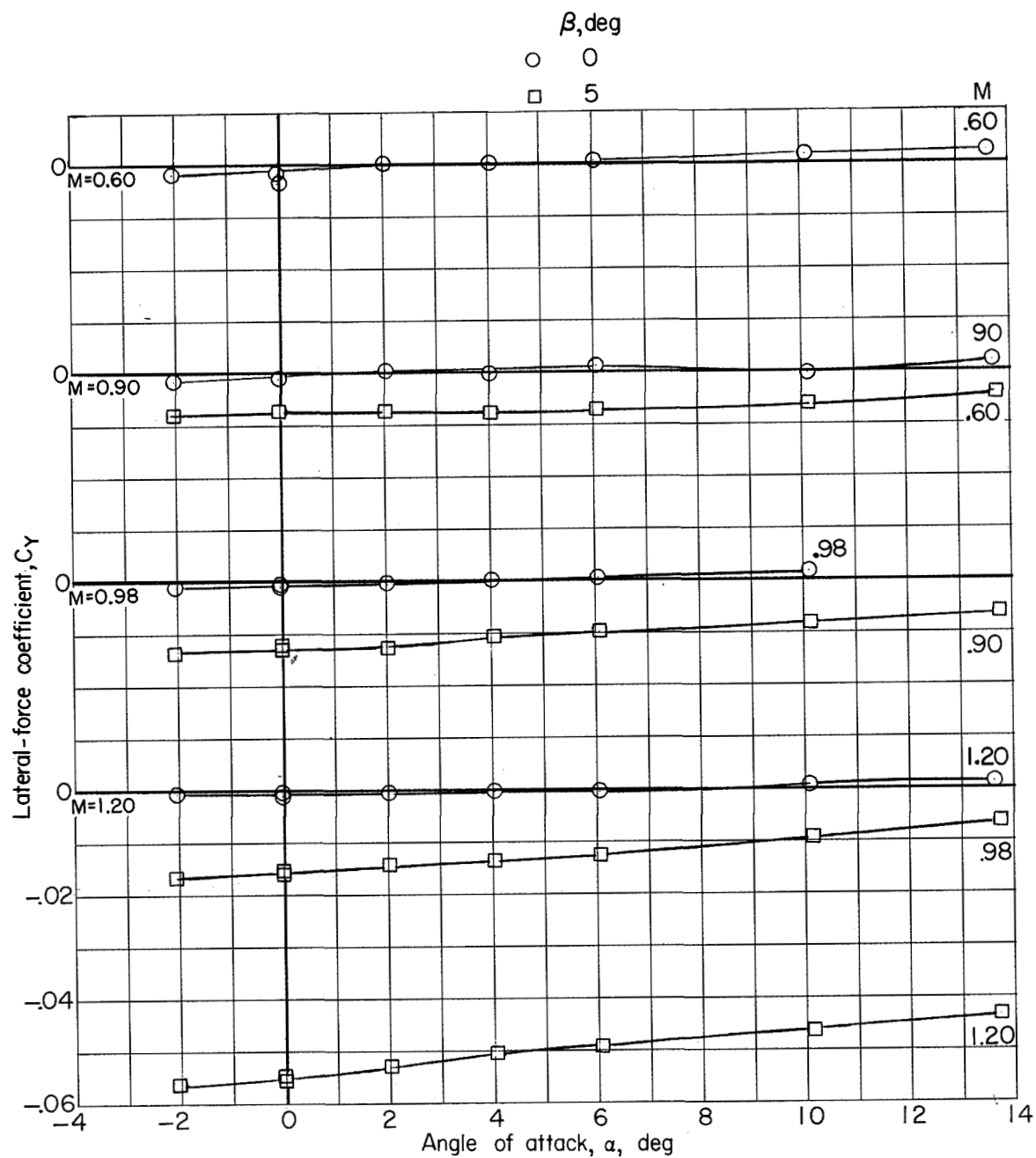
Figure 9.- Continued.



(e) Yawing-moment coefficient plotted against angle of attack.

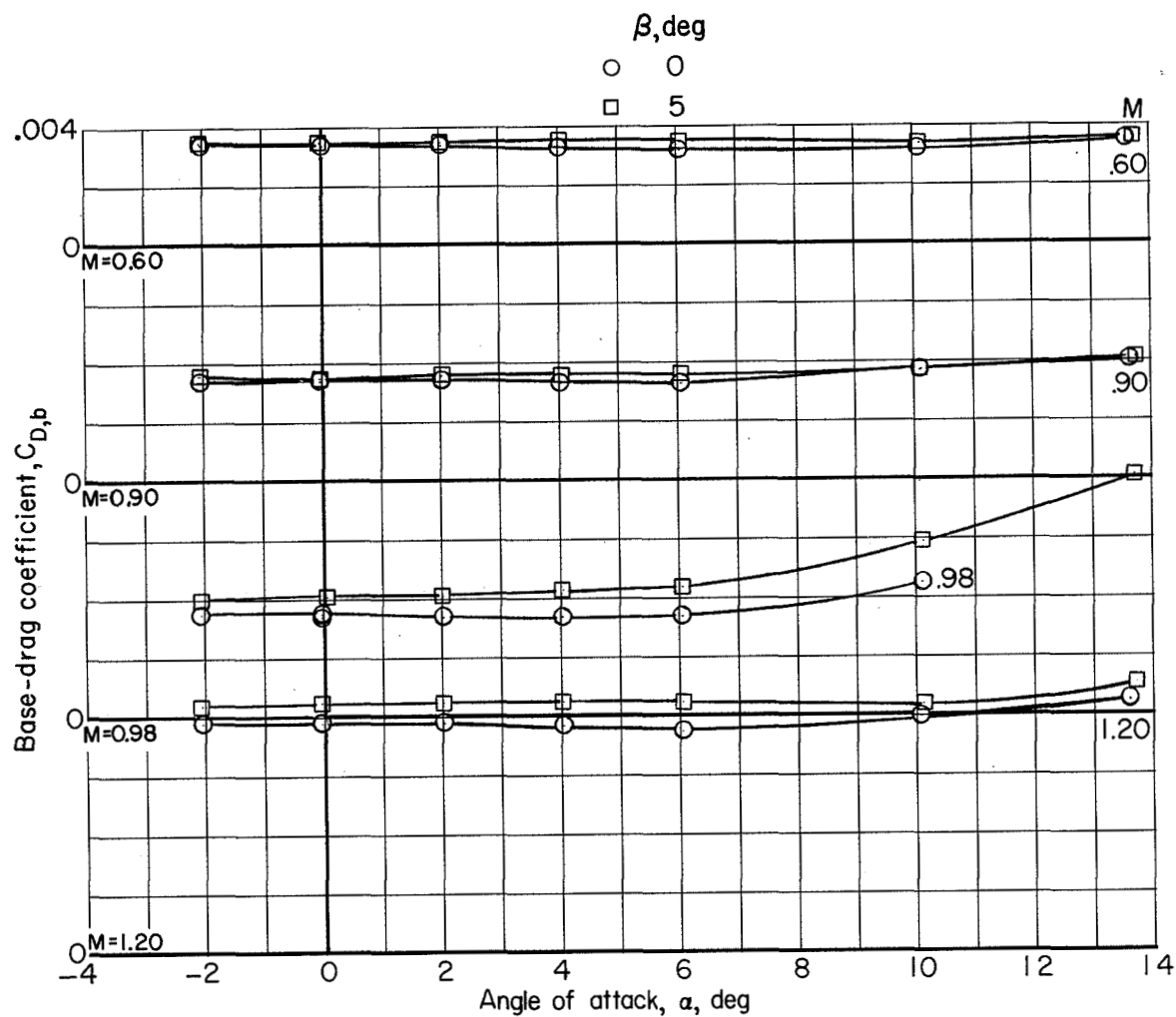
Figure 9.- Continued.





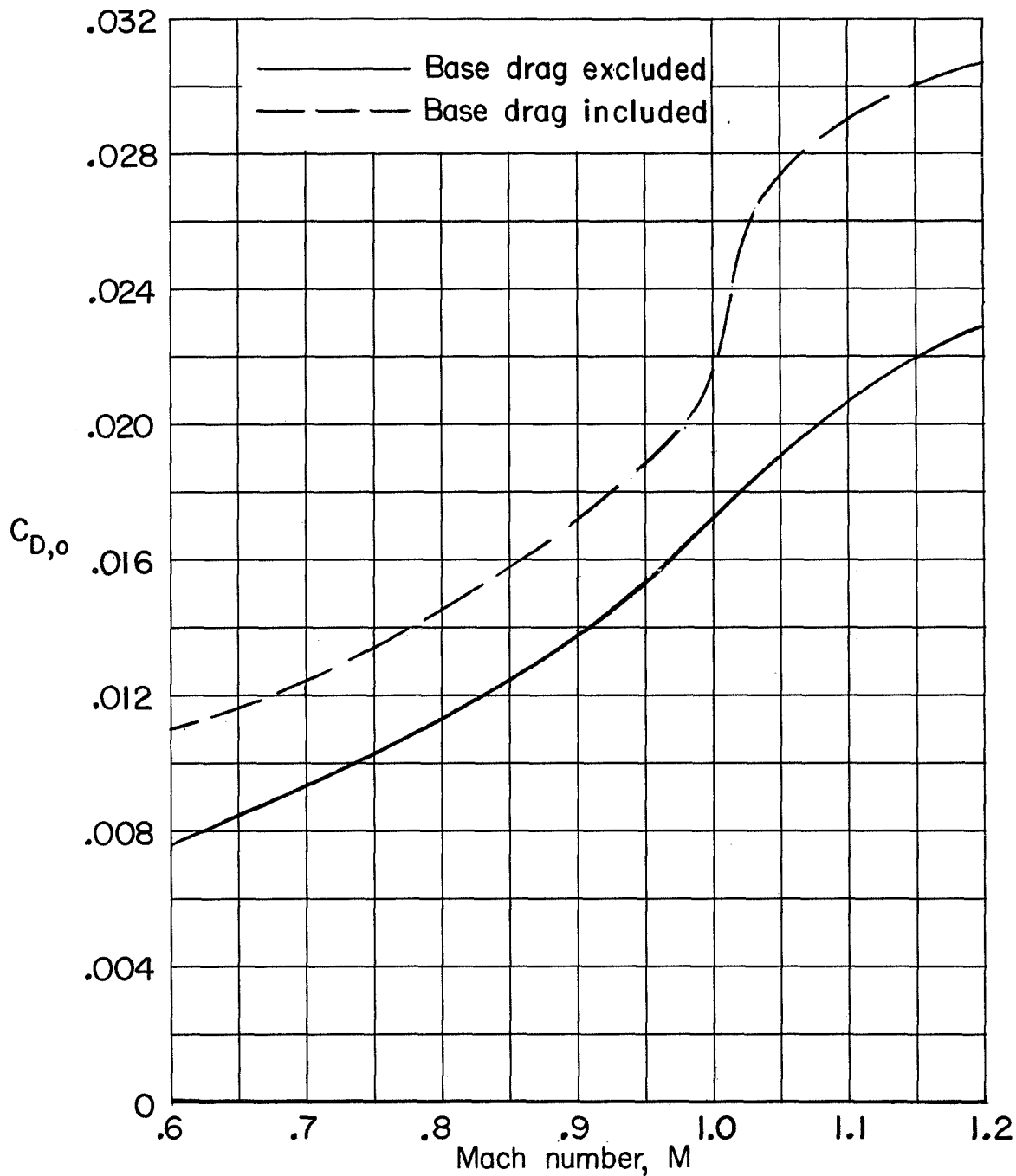
(f) Lateral-force coefficient plotted against angle of attack.

Figure 9.- Continued.



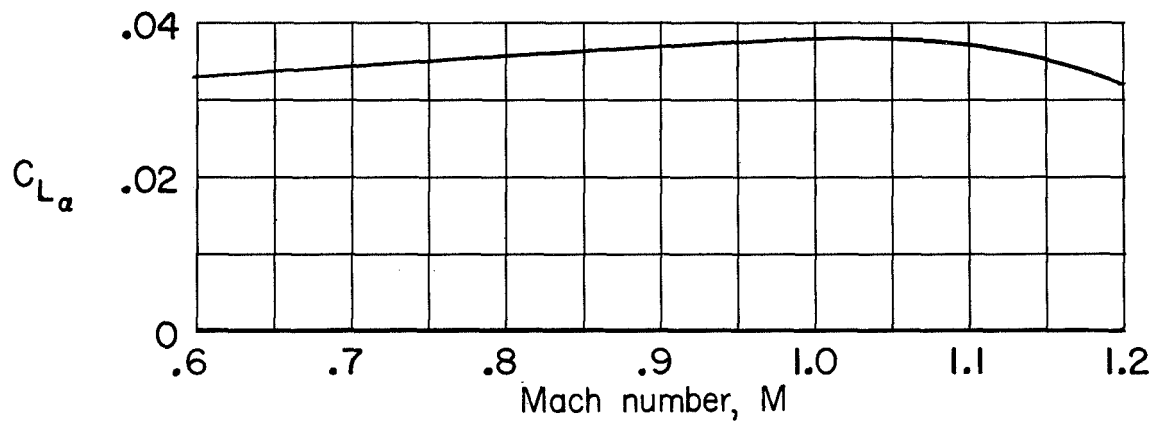
(g) Base-drag coefficient plotted against angle of attack.

Figure 9.- Concluded.

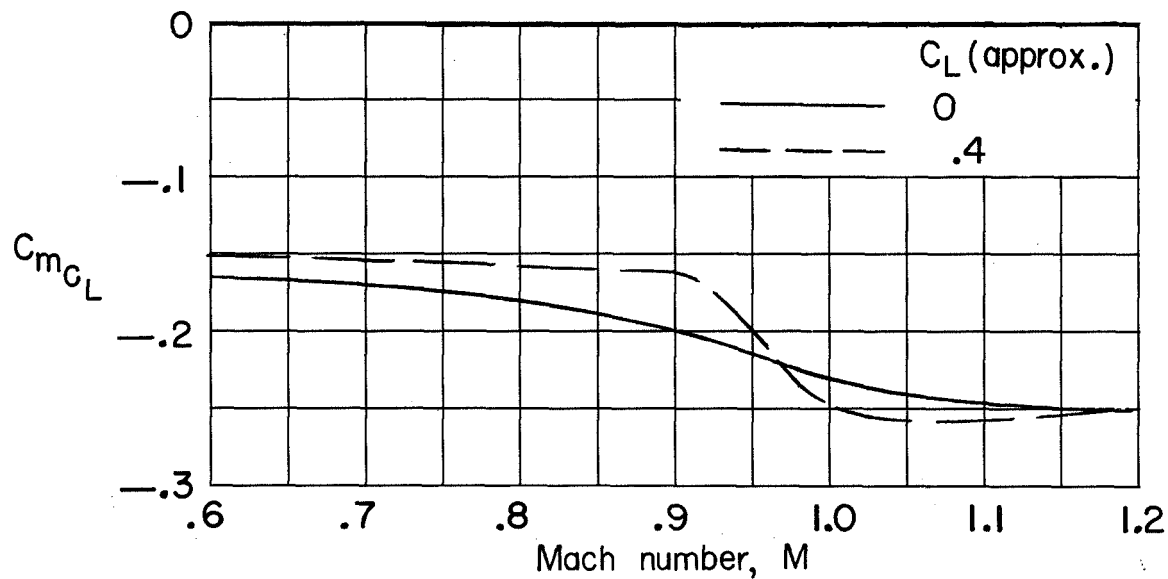


(a) Drag coefficient at zero lift plotted against Mach number.

Figure 10.- Variation with Mach number of the drag coefficient at zero lift and the longitudinal stability parameters for the recoverable booster alone.  $\beta = 0^\circ$ .



(b) Lift-curve slope plotted against Mach number.



(c) Longitudinal stability parameters plotted against Mach number.

Figure 10.- Concluded.



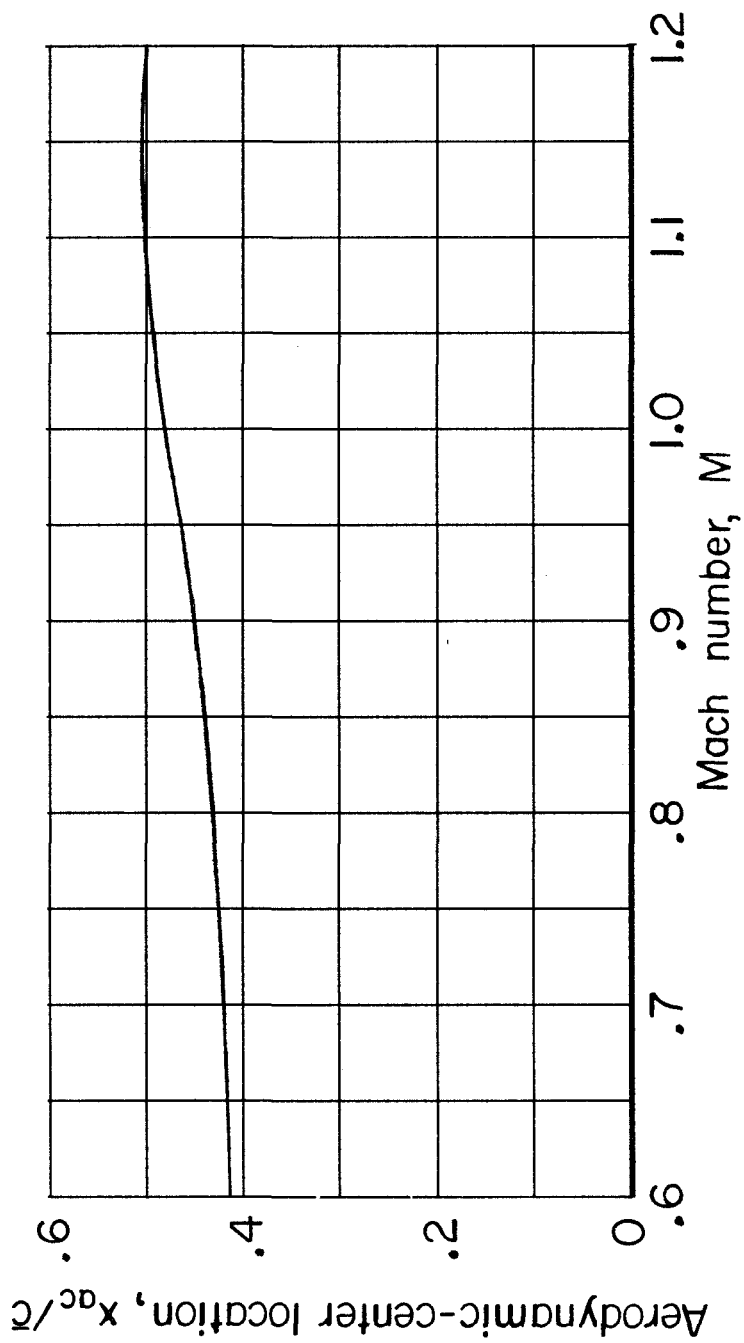


Figure 11.- Variation with Mach number of the aerodynamic-center location for the recoverable booster alone.

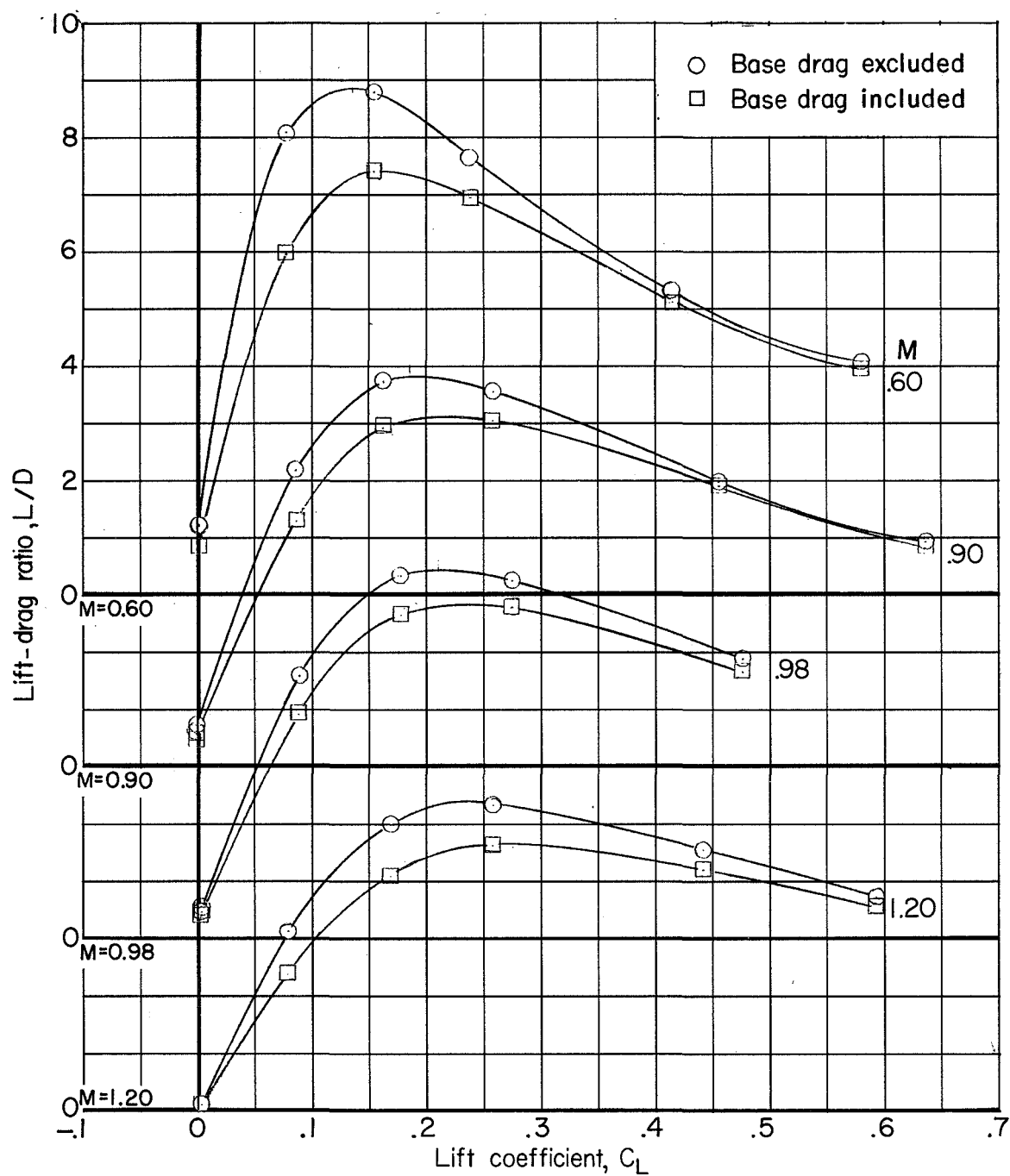


Figure 12.- Variation of the lift-drag ratio with lift coefficient for recoverable booster alone.

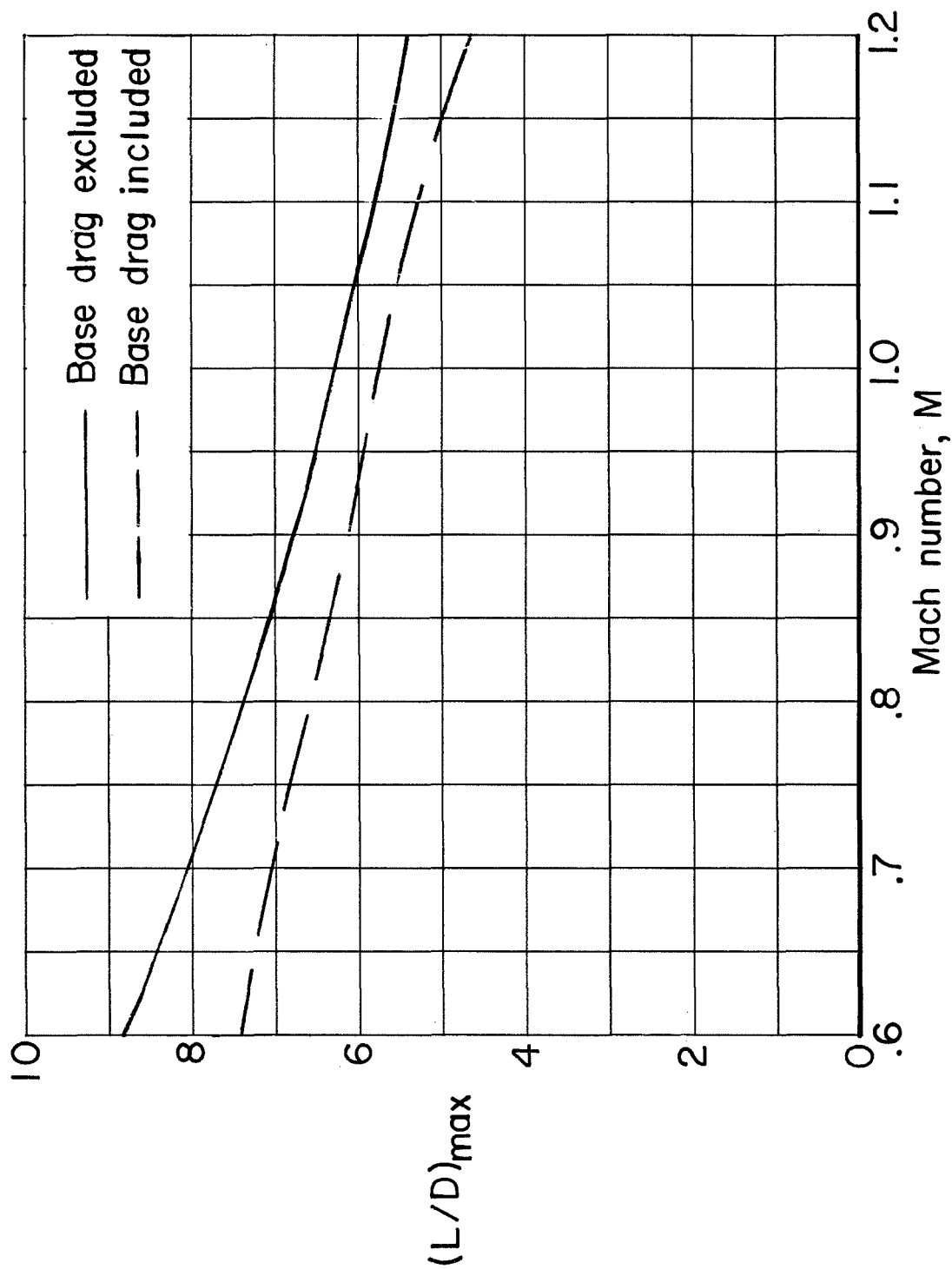
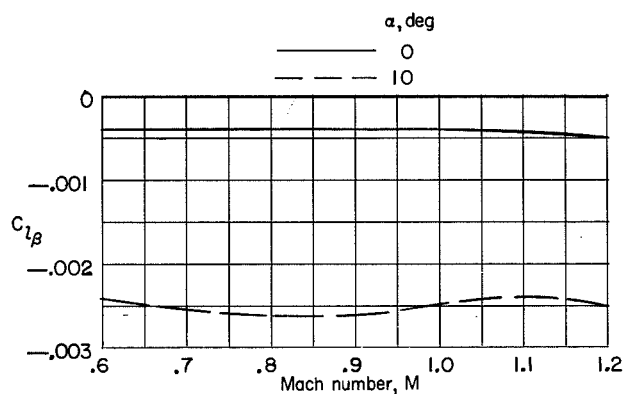
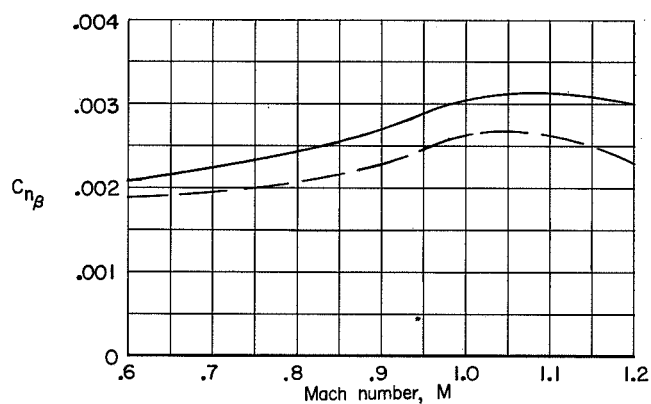


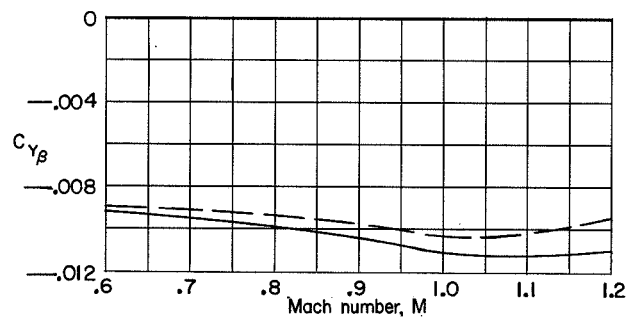
Figure 13.- Variation with Mach number of  $(L/D)_{\max}$  for the recoverable booster alone.



(a) Effective dihedral parameter plotted against Mach number.



(b) Directional stability parameter plotted against Mach number.



(c) Lateral-force parameter plotted against Mach number.

Figure 14.- Effect of angle-of-attack variation with Mach number on the lateral-directional stability parameters for the recoverable booster alone.